

Cloud Structure and Physical Conditions in Star-forming Regions from Optical Observations. I. Data and Component Structure

K. Pan,^{1,2,3} S. R. Federman,^{1,2}

Department of Physics and Astronomy, University of Toledo, Toledo, OH 43606

K. Cunha,

Observatorio Nacional - MCT, Rua Gal Jose Cristino 77, Rio de Janeiro, Brazil CEP
22921-400

V. V. Smith,

Department of Physics, University of Texas at El Paso, El Paso, TX 79968
and McDonald Observatory, University of Texas at Austin, Austin, TX 78712

and

D. E. Welty^{1,2}

University of Chicago, Astronomy and Astrophysics Center, 5640 South Ellis Ave.,
Chicago, IL 60637

Received _____; accepted _____

¹Guest Observer, McDonald Observatory, University of Texas at Austin.

²Visiting Observer, Kitt Peak National Observatory, National Optical Astronomy Observatories, which is operated by AURA, Inc., under cooperative agreement with the National Science Foundation.

³Current address: Department of Physics and Astronomy, Bowling Green State University, Bowling Green, OH 43403

ABSTRACT

We present high-resolution optical spectra (at $\sim 0.6\text{--}1.8 \text{ km s}^{-1}$) of interstellar CN, CH, CH^+ , Ca I, K I, and Ca II absorption toward 29 lines of sight in three star-forming regions, ρ Oph, Cep OB2, and Cep OB3. The observations and data reduction are described. The agreement between earlier measurements of the total equivalent widths and our results is quite good. However, our higher resolution spectra reveal complex structure and closely blended components in most lines of sight. The velocity component structure of each species is obtained by analyzing the spectra of the six species for a given sight line together. The tabulated column densities and Doppler parameters of individual components are determined by using the method of profile fitting. Total column densities along lines of sight are computed by summing results from profile fitting for individual components and are compared with column densities from the apparent optical depth method. A more detailed analysis of these data and their implications will be presented in a companion paper.

Subject headings: ISM: clouds — ISM: structure — ISM:molecules — Stars: formation

1. INTRODUCTION

The interstellar medium (ISM) is not static as was thought during the early part of 20th century. It is the reservoir out of which stars are born and into which stars inject newly created elements as they age. The physical and chemical state in the ISM continuously changes by the combined actions of star formation and stellar death (Cox & Smith 1974; Jenkins & Meloy 1974; Burstein 1977). The evolution of a galaxy is governed to a large

extent by these processes. The final stages of star formation involve the disruption of interstellar material from which stars form. If enough material is available in interstellar clouds forming O and B stars, one generation of stars can initiate the formation of a second generation, and so forth, but eventually the cloud remnants will no longer be able to sustain star formation. The propagation of star formation occurs in regions of enhanced gas density behind shocks (Elmegreen & Lada 1977). Phenomena associated with O and B stars that lead to shocks in the surrounding medium include stellar winds, expanding H II regions, and supernova explosions. Since O and B stars tend to form in clusters, these effects are magnified; the prodigious star formation seen in the Magellanic Clouds is an example of these processes. Clearly, knowledge of the physical conditions and chemical composition of the ISM in star-forming regions will help us understand the above processes, in particular, and the evolution of the ISM and the Galaxy in general.

Determination of the physical properties and chemical transitions of individual interstellar clouds from observations of absorption lines requires high-resolution spectra. High resolution is needed to distinguish the individual components contributing to the generally complex absorption-line profiles seen in most lines of sight. Most previous studies utilized one of two complementary approaches. One approach relies on a comprehensive analysis of the atomic and molecular material observed along a specific line of sight toward a background star. The objective here is the determination of cloud structure, density, and temperature for the gas and of the flux of ultraviolet radiation permeating the cloud. Efforts in this vein include analyses of gas toward ζ Oph (Black & Dalgarno 1977; van Dishoeck & Black 1986), γ Ara (Federman & Glassgold 1980), HD 169454 (Januzzi et al. 1988), HD 29647 and HD 147889 (van Dishoeck & Black 1989), and HD 37903 and HD 147009 (Knauth et al. 2001). The second approach focuses on a single species through observations of many lines of sight. Previous studies of this kind examined the chemistry of CO (Federman et al. 1980), of CH (Federman 1982; Danks, Federman, & Lambert 1984;

Crawford 1989), and of CN (Federman, Danks, & Lambert 1984). The main goals of these investigations are to study the chemistry of observed species and to put constraints on chemical and physical conditions in clouds.

In the present study, we combine the two approaches. Interstellar material toward 29 lines of sight in three star forming regions, ρ Oph, Cep OB2, and Cep OB3, is probed through a study of absorption lines against the continua of background stars. High-resolution optical spectra ($\delta v \sim 0.6\text{--}1.8 \text{ km s}^{-1}$) of six species, CN, CH, CH^+ , Ca I, K I, and Ca II are obtained for each line of sight. The present study provides the most complete picture of the physical conditions and cloud structure in the diffuse molecular gas associated with the three star-forming regions. While many observations of radio emission from these three regions have been made, the much better sensitivity of absorption line studies allows us to observe gas components with lower molecular column density that radio observations cannot find and to reveal small-scale cloud structure that radio observations did not uncover. On the other hand, comparison of the absorption line measurements to the large scale CO radio observations can help us understand the large-scale structure of clouds.

In this paper, we present the optical spectra for the three star-forming regions. In §§ 2 and 3, we describe the procedures to obtain, reduce, and analyze the spectra. A more detailed analysis of these spectra and their implications will be presented in a companion paper (Pan et al. 2003).

2. OBSERVATIONS AND DATA REDUCTION

2.1. Program Stars

Observations of absorption from interstellar gas require the use of a bright, ideally, rapidly rotating star, as the light source; sharp interstellar absorption lines are then

superposed on broader stellar features. Typically, there are multiple interstellar clouds (or cloud clumps) along a given line of sight whose existence is revealed by absorption at distinct Doppler velocities. In order to study cloud structure and physical conditions of the clouds associated with ρ Oph, Cep OB2, and Cep OB3, interstellar CN, CH, CH⁺, Ca I, K I, and Ca II absorption was sought in 29 sight lines.

Our target list is based on earlier stellar and interstellar studies (e.g., Federman et al. 1994; Patel et al. 1998; Daflon et al. 2001). Stellar data for the program stars are listed in Table 1. In particular, the HD number, name, spectral type, V , Galactic coordinates, reddening, and distance are given. The values of $E(B - V)$ are from Blaauw et al. (1959), Simonson (1968), and Garrison & Kormendy (1976), and the distances are estimates from a combination of Hipparcos measurements (Perryman 1997) and spectroscopic parallax using data from Allen (1973). Other parameters are from the Simbad Database, operated at CDS, Strasbourg, France. An additional selection criterion for Cep OB2 was the position of the line of sight relative to cloudlets seen in CO radio emission (Patel et al. 1995, 1998).

Spectra were acquired at two sites. Brighter stars were observed with the 0.9 m Coudé Feed Telescope at Kitt Peak National Observatory (KPNO), while fainter stars were observed with the 2.7 m telescope at McDonald Observatory of the University of Texas at Austin. Data on three stars, ρ Oph A, HD203374A, and HD206773, were obtained at both sites, thereby providing a check on consistency. Additional observations of stars in Cep OB2 were obtained with the Sandiford echelle spectrograph on the 2.1m telescope at McDonald Observatory; details about data reduction can be found in Daflon et al. (2001). These spectra included the wavelength range sampling CH, CH⁺, and Ca I absorption. Interstellar equivalent widths for sight lines from this data set, but not studied at high spectral resolution, are given in the Appendix.

2.2. KPNO Spectra

Interstellar spectra for 12 program stars were obtained at KPNO during four runs in 1995 (September 28—October 5), 1996 (September 4—5), 1999 (October 30—November 8), and 2000 (September 9—12). Three instrumental setups were used in order to get CN, CH, CH^+ , Ca I, K I, and Ca II absorption features for these lines of sight.

Two configurations were used for blue settings. The first setup was for interstellar CN $\lambda 3874$ and Ca II $\lambda 3933$ absorption. To achieve the desired high spectral resolution ($\sim 1.5 \text{ km s}^{-1}$), we used the echelle grating in 143th order centered near 3943 Å, cross dispersed via grism 780-2 in 2nd order, camera 6, and a 90 μm entrance slit, corresponding to 0.⁶ on the sky. A CuSO₄ filter was used to eliminate the grism's 1st order contributions, and a 3° wedge positioned the desired spectral region on the F3KB CCD (1024×3072, 15 μm pixels) detector. Exposures were binned by 2 pixels perpendicular to the dispersion. For the second setup, interstellar absorption features of CH $\lambda 4300$, $\text{CH}^+ \lambda 4232$, and Ca I $\lambda 4226$ were obtained by centering the 132nd order of the echelle grating spectrum near 4273 Å, keeping other settings the same as in the first setup. Grism 730 instead of 780-2 was employed, and no wedge was used for this setup in 1995.

A third setup was used to acquire interstellar K I $\lambda 7699$ features by centering the 73rd order of the echelle grating spectrum near 7700 Å. In this setup, an RG-610 blocking filter was used. The entrance slit width was changed to 100 μm . Other settings were the same as in the second setup.

In addition to stellar images, a variety of exposures were made for the purpose of calibration. Fifteen zero and flat lamp exposures, and a few Th-Ar hollow cathode lamp exposures, were taken each night. Five dark exposures were made during each observing run. The zero exposures were used to remove the bias voltage in the CCD detector. Flat lamp frames measured the variation in sensitivity from pixel to pixel across the CCD

chip. The Th-Ar comparison exposures provided the wavelength scale for the extracted interstellar spectra. Dark frames gave the maximum contribution from thermal noise, which was subtracted from stellar exposures when necessary. Moreover, the echelle grating was moved slightly each night in order to reduce the effect of any flat field artifacts. The setups yielded spectral resolutions of about 1.3 to 1.5 km s^{−1}, as determined from the full widths at half maximum (FWHM) of the thorium lines in the comparison spectra assuming intrinsic widths of the lines are about 0.55 km s^{−1} (Welty et al. 1994).

2.3. McDonald Observatory Spectra

Twenty stars were observed with the 2dcoudé spectrograph (cs21) (Tull et al. 1995) on the 2.7 m telescope during three runs in 2000 (September 3—8) and 2001 (July 7—13; August 29—31). Grating E1 and the TK3 CCD were used for the observations. A cross-dispersed echelle spectrometer and the availability of a 2048×2048 CCD made it possible to get CN, CH, CH⁺, Ca I, and Ca II absorption features in a single exposure by setting the cross disperser to its 2nd order, and by centering the 56th order of the echelle grating spectrum to 4065 Å. K I λ 7699 spectra were obtained by setting the cross disperser to its 1st order and by centering the 31st order spectrum to 7165 Å. Slit # 2 with a width of 145 μ m was used for all observations. An exposure time of 30 minutes per stellar image for faint stars was chosen to limit the effect of cosmic rays during the data collection process.

As we did in KPNO observations, a variety of auxiliary exposures were taken for calibration purposes. Typically, four or five dark exposures were made for each observing run. Twenty zeros and ten flat lamp exposures were taken each night. Th-Ar comparison frames were taken throughout each night, usually every two hours. The measured width of thorium emission lines in the comparison spectra indicates a resolution of about 1.7 km s^{−1} for these observations.

Higher resolution spectra, of about 0.56 km s^{-1} , for K I toward 9 Cep, ν Cep, and λ Cep, and for Ca I toward λ Cep were obtained with the same telescope and a double-pass configuration in 1995 and 1996 (for details of the instrumental setup, see Welty & Hobbs 2001; Welty, Hobbs, & Morton 2003). These spectra are labeled as M2 in Figures 1—15.

2.4. Data Reduction

The raw image data from both telescopes were reduced in the usual manner with the NOAO IRAF (Image Reduction and Analysis Facility) package. Flat field frames were first examined to determine overscan and data regions, while object and bias frames were examined to locate abnormal (dead or hot) pixels. Stellar, flat, and comparison frames were bias-corrected by subtracting the average bias exposure from them. Cosmic-ray hits were removed from stellar images. Scattered light was fitted by low-order polynomials, in both the dispersion direction and perpendicular to it for the multi-order echelle data, and removed from each stellar and flat field exposure. The normalized average flat field was divided into the stellar images to account for differences in pixel-to-pixel sensitivity. Since each echelle order was a few pixels wide, the orders were summed across this width without weight. Then all extracted one-dimensional spectra were calibrated in wavelength using the Th-Ar comparison spectra, and were Doppler-corrected. Spectra with interstellar absorption lines and sufficient continua on both sides, usually 2 \AA , were cut from each stellar exposure. Each spectrum was carefully examined for flat field artifacts and cosmic ray blemishes that remained. The cosmic ray blemishes were subsequently removed unless the blemishes coincided with interstellar lines; then that spectrum was excluded in the final summation. After the examination, spectra for the same species toward the same star were summed together to obtain a final spectrum with higher signal-to-noise ratio, SNR, typically about 50 to 150. The stellar continua were normalized by fitting low order Legendre

polynomials to regions free of interstellar absorption. This continuum normalization was easily performed except for a few cases, such as Ca II toward ν Cep, 9 Cep, and 13 Cep where interstellar features were superposed on strong, relatively narrow stellar absorption lines. As a result, higher order polynomials had to be used there. The data reduction for K95, K96, M95, and M96 spectra is somewhat different (see Welty & Hobbs 2001 for details).

The data reduction procedure used here is slightly different from the one employed by Pan et al. (2001). Instead of median smoothing, the **cosmicrays** routine was used to remove cosmic-ray hits, bad CCD columns were fixed by linear interpolation from neighboring columns, and all frames were overscan debiased prior to average-bias subtraction. The new procedure yielded more satisfactory continua. The overall shapes of line profiles did not change, although line profiles were slightly deeper in some cases because the original smoothing broadened lines artificially. We were able to discover a few weak components that were not visible with the original procedure. However, Pan et al.’s (2001) conclusions are not altered by the improved extraction.

The final normalized interstellar spectra for CN, CH, CH^+ , Ca I, K I, and Ca II are shown in Figures 1 through 15. The spectra are shown in V_{LSR} space. To facilitate comparisons between profiles, all the K I and Ca II spectra are on the same vertical scale, but the scales for weaker lines may differ from panel to panel.

3. ANALYSIS AND RESULTS

3.1. Total Equivalent Widths

Some of our program stars were observed previously, usually at lower resolution; total equivalent widths (W_λ) along a line of sight were given. In order to compare our results

with the previous values of W_λ , we also measured total equivalent widths for all six species. Tables 2—4 list our measurements along with their uncertainties and previous W_λ values from the literature. Three stars, ρ Oph A, HD203374A, and HD206773, were observed at both McDonald and Kitt Peak. Therefore, two measurements exist for all species toward them except for CH toward ρ Oph A, for which we had only McDonald spectra, and for K I toward HD203374A and HD206773, which were observed at Kitt Peak only. The first rows for the three stars are W_λ values from McDonald spectra, and the second rows are from Kitt Peak observations. As one can see from the Tables, the equivalent widths measured from McDonald and Kitt Peak spectra agree very well.

The listed uncertainties are only those associated with random noise in the continua and the width of the profile. Systematic uncertainties due to continuum placement and other factors in the present dataset are not included. Typically, uncertainties in total W_λ values caused by misplacements of continua are 5% for weak lines and 2-3% for strong ones. Considering these uncertainties, our total equivalent widths agree very well with previous measurements. Among our 228 measurements, 100 have previous W_λ values. Only 3 of them show statistically significant discrepancies: Ca II toward HD206165 (248.1 vs. 321 mÅ); CN R(0) toward HD206165 (6.5 vs. < 3 mÅ); and CN P(1) toward ρ Oph C (3.3 vs. 9.2 mÅ). Three others, Ca I toward HD208905, HD209339, and HD209481, indicate possible disagreement with absolute W_λ differences of about 4.0 mÅ.

Of the 3 discrepant cases, the difference in CN P(1) of ρ Oph C is most likely due to errors in the previous measurement (Federman, unpublished). The measurement gave consistent equivalent widths for the stronger CN R(0) and R(1) lines but a higher W_λ for P(1). Furthermore, the W_λ value for P(1) is larger than the equivalent width for R(1), an unphysical situation. The other two differences involve HD206165. It is difficult to make a firm statement. The difference in Ca II toward this star could be due to differences in

recognizing the strong stellar line, on which the interstellar Ca II feature is superposed. However, this can not explain the disagreement in CN. It is possible that the differences may be caused by small-scale variation along the line of sight. The proper motion of HD206165 is about 3.4 mas yr⁻¹. The time span between our observations and the previous one (Chaffee & Dunham 1979) is about 25 yrs, corresponding to an 85 AU separation at a distance of about 1000 pc. Evidence for pervasive small-scale structure on this scale has been found from ultraviolet, optical, and radio observations (e.g., Frail et al. 1994; Lauroesch & Meyer 1999; Pan et al. 2001; Welty & Fitzpatrick 2001). Furthermore, the previous measurement (Chaffee & Dunham 1979) also reported a higher Ca I W_λ value, 12 mÅ, compared to ours of 7.8 mÅ.

3.2. Component Structure

Our spectra clearly exhibit multiple velocity components in each line of sight, as seen in Figs. 1 to 15. Each interstellar line profile carries information about the number of velocity components, column density (N), the wavelength (λ) or velocity (V) at line center, and line width (b -value, $\sim \text{FWHM}/1.665$) for each component. We used the method of profile fitting to determine column densities, line widths, and velocities of individual components contributing to the observed absorption line profile. The program FITS6P (Welty, Hobbs, & York 1991) was used for this purpose. We determined the component structure by analyzing spectra of all the observed species for a given line of sight together. Therefore, our component structure of each species is also constrained by spectra of other species for the same line of sight.

If only one component is present, the profile is assumed to be symmetric, and the determination of its λ , b -value, and N is straightforward. The wavelength can be determined from the centroid of the line profile; W_λ and line width can be measured by fitting a single

Gaussian or Voigt profile. Then the column density can be derived by using curves of growth. However, if a line profile consists of multiple components, the task of determining λ and W_λ of each component is considerably more difficult if the components are not completely resolved. The task could be even harder when the absorption features become saturated. Unfortunately, the latter is the case for most of the K I and Ca II measurements. Typically, there are more than 10 velocity components in a Ca II profile and 7 in a K I spectrum for each line of sight. Furthermore, the central components are usually quite saturated. Therefore, it is very difficult to extract the component structure from only K I and Ca II spectra. On the other hand, CN, CH, CH^+ , and Ca I spectra provide information on V_{LSR} for the strong K I and Ca II components because the distributions of different species in the same line of sight are related more or less. For instance, if there is a CN component at a certain V_{LSR} , we would expect a CH component at that V_{LSR} . The same is true for CH and K I. Among our observed species, Ca II is the most widely distributed. If any other species has a component at a specific V_{LSR} , presumably, Ca II will have a corresponding component at that velocity. Thus, V_{LSR} information for strong Ca II components can be obtained by measuring spectra of other species for which the lines are not saturated. Usually, the central wavelengths of weak components on both shoulders of a Ca II line profile can be determined relatively well by examining the line profile itself. Therefore, by analyzing spectra of all species together, component structure of each species is much better constrained than when it is determined from a spectrum for only one species. With a well-defined component structure, reliable column densities and line widths for each component can be extracted from the spectra. In all measurements, we adopted the minimum number of components needed to fit the observed line profiles adequately, given the SNR achieved in each case. In a few cases, velocity offsets from one species to another were recognized by a common difference for all components; they were treated in the fitting procedures. Table 5 displays adopted component structures for all

species; the LSR velocities given in column 1 represent an average from the suite of fits.

Different species may trace regions of a cloud where physical conditions are different, or sometimes even different clouds. For instance, CN traces dense gas. Some clouds are not dense enough to have detectable CN lines. As expected, among the six species, the CN profile is usually much less complicated than profiles of other species for a given sight line. This makes the CN spectrum a good starting point for the analysis.

In our CN spectra, there are at most 5 velocity components for a given line of sight. They are usually well resolved and far from saturated. Thus, CN component structures can be determined adequately by profile fitting the CN spectrum itself in most cases. We started the analysis by examining the symmetry and width of the CN line profile. If the CN feature was symmetric, we first attempted one-component fitting. If the fitted profile was not very broad, we proceeded with one component fitting. If the fitted profile was too broad, i.e., its corresponding Doppler parameter, b -value, is greater than our set limit of 1.6 km s^{-1} (discussed below), we examined CH and K I spectra for the sight line, and tried to find constraints from them. Usually we ended up with multiple (in most cases, two) CN components. An asymmetric line profile is a telltale sign of the presence of multiple components along a line of sight. If the CN profile is asymmetric, multiple component structure was adopted. The goodness of a fit was checked by examining the residuals. We ensured that residuals, after subtracting the fitted profiles, were indistinguishable from the noise in the continuum. The FITS6P program outputs N , b -value, velocity, and W_λ of individual components. The second and third columns of Table 5 list the derived N and b -value of each CN component.

It is rather difficult, if not impossible, to find the unique “true” component structure of a complicated profile from profile fitting because of spectrum noise, not high enough spectral resolution, and too many free parameters that we have to fit. As stated above,

we may be able to constrain the number of components by analyzing spectra of other species, but this is not always the case. Therefore, we set the following b -value limits for components of different species in our analysis. For CN, the limit was 1.6 km s^{-1} , which is two times mean b -values found by Gredel et al. (1991) and 2.5 times average b -values found by Crane et al. (1995). It was 2.0 km s^{-1} for CH, Ca I, and K I, which is two times the b -values adopted by Knauth et al. (2001) and 3 times median b -values obtained by Welty et al. (2003) and Welty and Hobbs (2001). A limit for CH^+ and Ca II of 3.5 km s^{-1} , 1.0 km s^{-1} greater than those adopted by Knauth et al. (2001), was chosen. We point out that these limits played at most a minor role in our analysis because there were few instances requiring them.

Once the CN component structure was obtained for a line of sight, we analyzed the CH profile for the sight line. First, we examined CH components that could be well defined by working on the CH spectrum itself. If all components could be adequately determined in this simple way, our next step was to check whether all CN components were present in the CH profile. If not, an iteration was performed to ensure the CH profile included all CN components. A V_{LSR} difference of $\lesssim 0.3 \text{ km s}^{-1}$ between CH and CN components was considered a match (i.e., the same component was detected in both species). In some cases, CH profiles were not so simple. Usually, only the central wavelengths (velocities) of weak components on the sides of a CH profile could be defined adequately. The strong CH components, whose corresponding CN are usually detected, were blended. Fortunately, we have V_{LSR} (or central wavelength) for these strong CH components from CN, and we adopted velocities from CN for strong CH components as our initial input to FITS6P. In some cases, we had to add additional CH components, which neither were seen in CN nor identified through examination of the CH profile, in order to fit the data adequately. The effects of Λ -doubling on the CH line was included in profile fitting. The inferred column densities and b -values of CH components are listed in the fourth and fifth columns of Table

5.

The CH^+ and Ca I structures were studied next because they are useful in interpreting K I and Ca II profiles. Usually, CH^+ and Ca I lines are not saturated. With the aid of the CH component structure, CH^+ and Ca I components were not too difficult to define. Although we fit line profiles of these two species so that they could share common velocity components with other species (analyzed to this point), none of the component structures for the two species was required to contain the structure for other species in its subset. The fitted N and b -values for CH^+ and Ca I components are in columns 6 to 9 of Table 5.

K I components were determined with the aid of the CH, CH^+ , and Ca I component structures. Because more components were present in K I line profiles (as many as 10 in our spectra), their analysis is more difficult than for CH. In a few cases, we had to go through iterations from CN and CH to K I profile fitting in order to get an adequate fit with reasonable widths, and to make the CH component structure a subset of the K I structure for a given line of sight. HD207308 is one such case. The CN line profile for this line of sight looks “symmetric”. We first attempted to fit it with one component. The one-component fitting yielded a fairly large line width with a b -value of $\sim 1.5 \text{ km s}^{-1}$. Since it was still slightly smaller than the b -value limit set for CN (1.6 km s^{-1}), we started the CH analysis with one CN component. However, we could not get consistent CN, CH, and K I component structures. Only when the CN line profile was fit by two components did we get consistent results for all three species. Moreover, the b -values of the two CN components dropped to more typical values, 1.0 and 0.9 km s^{-1} , respectively. Therefore, we feel more confident with this two-component structure. This analysis highlights how using spectra of several species together aids in obtaining reliable component structure for all species. The hyperfine splitting of K I $\lambda 7699$ was considered in the profile fitting. The derived K I column density and b -value of each component are tabulated in the 10th and 11th columns

of Table 5.

The Ca II line profile was the most difficult one to study, not only because more components were present, but also because the Ca II components are more saturated. We see as many as 25 components in a Ca II spectrum for a line of sight. In a few cases, the relative intensities of the Ca II line profiles almost reached zero, as low as 10^{-3} , though they never became black. The Ca II spectra were fitted by using the same method as the one employed for the K I measurements. However, in some cases, iterations were again performed to ensure consistent component structures for a given line of sight—i.e., velocity components seen in another species would appear in the Ca II structure. Of course, Ca II can have extra components not detected in any of the other observed species. The N and b -values of Ca II components are given in the last two columns of Table 5.

As mentioned earlier, four spectra, K I $\lambda 7699$ toward 9 Cep, ν Cep, and λ Cep, and Ca I $\lambda 4226$ toward λ Cep, had much higher spectral resolution ($\sim 0.6 \text{ km s}^{-1}$) than others ($\sim 1.5 \text{ km s}^{-1}$). For consistency, we smoothed the higher resolution spectra before further analysis so that they had comparable resolution to the spectra of other species for these lines of sight.

Because some K I and Ca II components were strong, even quite saturated, we could hardly extract useful information on how many nearby components are present by examining the K I and Ca II profiles alone. As stated above, we calculated the central wavelengths of these strong components using information from spectra of other species (such as CH^+ , CH) in the same line of sight. Then we fit multiple Voigt profiles to the K I and Ca II line profiles by using the calculated central wavelength as initial input. However, there could be weak components (blended with strong ones) in line profiles not seen in other species. If this is the case, some closely blended weak components would be missed in our analyses. Since we did include some “additional” components in order to fit observed

data adequately, we believe all components with reasonable strengths were found.

One advantage of our study is that we observed six species for each line of sight with instruments having the same or similar resolutions, and reduced the data in the same fashion. By analyzing spectra of six species for a given line of sight together, we obtained consistent velocity component structures for all species. Therefore, we believe that the derived component structures, as well as the N and b -value for each component, are more reliable than those deduced from a single species.

There are factors that could introduce uncertainties into the derived column densities, b -values, and velocities. Uncertainties associated with noise in the spectra and placement of continua can be estimated whereas errors due to other factors, such as zero point offsets from one species to another in the profile fitting, may be rather difficult to quantify. For well defined intermediate strength components, the formal 1σ uncertainties in column densities are typically $\lesssim 5\%$, comparable to the uncertainties that would be inferred from the errors bars on equivalent widths associated with random noise in the spectra. The uncertainties in N can be 10 to 20% for strong but still well-defined components. As stated in §3.1, misplacements of continua may cause 5% uncertainties in equivalent widths for weak lines, and 2–3% for strong ones. For most components, the derived velocities and b -values have uncertainties of about 0.1 km s^{-1} , though they could be larger for broader and severely blended components. As noted above, component velocities derived from spectra of six observed species for a given line of sight agree within 0.3 km s^{-1} , a conservative measure of the accuracy in velocity. In the process of extracting component structure, we usually let velocities and widths of components vary independently. However, in a few cases, the b -value of certain component(s) or the velocity of component(s) were set during the profile fitting. In others, an offset from one species to another was recognized by a common difference for all components. These fitting restrictions and offset constraints could

introduce errors in N and b -value for some components. However, the b -values and velocities generally could not be changed by more than 0.2 km s^{-1} and 0.3 km s^{-1} , respectively, without noticeably degrading the fit. There is also the possibility of unresolved structure. In summary, uncertainties in our derived N are $\lesssim 20\%$ for most components, and somewhat larger for severely blended components. Typical uncertainties for b -values and velocities are 0.1 km s^{-1} . For significantly blended components, they are accurate to within 0.2 and 0.3 km s^{-1} , respectively.

3.3. Total Column Densities

Although we intend to interpret column density in term of velocity components rather than lines of sight, some studies based on lower resolution observations, such as *FUSE*, may need total column densities along lines of sight. The first column of each species in Table 6 lists our total column densities (hereafter FIT column density), based on summing the results of component structure along each line of sight. Comparison between these new total N obtained from detailed profile fits and previous values from total equivalent widths provide information on how reliable those earlier values are, and provide a connection to the majority of existing data.

Total column density along a line of sight can also be derived from the apparent optical depth method (Savage & Sembach 1991). An apparent optical depth, τ_a , is defined as a function of velocity,

$$\tau_a(v) = \ln \left[\frac{I_0(v)}{I(v)} \right], \quad (1)$$

where $I(v)$ is the recorded intensity and $I_0(v)$ is the continuum level. If τ_a is not very large, the differential column density per unit velocity is expressed as

$$N_a(v) = 3.768 \times 10^{14} \frac{\tau_a(v)}{f\lambda} \text{ cm}^{-2}(\text{km s}^{-1})^{-1}, \quad (2)$$

where f is the transition's oscillator strength and λ is the central wavelength in units of Å. A direct integration of the differential column density,

$$N_a = \int N_a(v)dv, \quad (3)$$

yields an instrumentally smeared column density. In principle, this instrumentally smeared column density is a lower limit to the true column. Savage & Sembach's (1991) simulations showed that the smeared column density is a good representation of the “true value” for weak and moderately strong absorption ($\tau \leq 0.5$). For strong absorption lines, the instrumental resolution plays an important role: For a single component with a maximum $\tau = 3.104$ (relative intensity down to 0.045), their calculations showed that the smeared column density was smaller than the “true value” by 8.4% when the instrumental resolution is 1.6 times broader than line width (b -value). Their simulations also indicated that the smeared column density was even closer to the “true value” in multiple component cases for a given maximum τ and instrumental resolution.

The apparent optical depth method makes no a priori assumptions regarding the velocity distribution of the absorbing gas, whereas profile fitting relies on component structures extracted from spectra of multiple species. As a check on our column densities and component structures, we obtained total column densities of each species using the apparent optical depth method for all sight lines (hereafter AOD column density). Results are listed in AOD columns of Table 6. FIT and AOD column densities for CN, CH, CH⁺, and Ca I agree within 3%, with FIT column densities generally slightly larger than their corresponding AOD column densities. For K I and Ca II, all FIT column densities are greater than AOD columns. The largest difference between FIT and AOD column densities

are 22% and 29% for K I and Ca II, respectively.

Although uncertainties in column densities for individual components can be 20%, uncertainties in total column densities for species for a line of sight are much smaller than that amount. Different component structure may cause column densities to change by 20% for some individual components, but total column densities of all components can not be changed more than 5% without noticeably degrading the fit. Therefore, we conclude that uncertainties in total FIT column densities are about 5%.

For CN, CH, CH^+ , and Ca I, where absorption is not strong and our instrumental resolution is comparable to the inferred line widths, the lower limit column densities set by the apparent optical depth method should not be far from the “true values” according to Savage & Sembach’s (1991) simulations. Therefore, the fact that the FIT column densities agree with, but are generally slightly greater than, AOD densities indicates that our FIT column densities are good representations of their “true values” for these species, and the component structures on which FIT column densities are based are reliable.

On the other hand, K I and Ca II absorption are usually much stronger, and their AOD column densities should be lower than their “true values”. In Table 6, FIT column densities are typically greater than AOD columns by 15% for K I, and by 5% for Ca II, except for the four lines of sight toward ρ Oph. While Ca II lines are deeper than K I lines, the AOD column densities for Ca II are closer to their FIT values. This reinforces our results that b -values for Ca II components are greater than those of K I. We note, however, that low SNR in the absorption cores of Ca II profiles may increase AOD column densities. For instance, if the relative intensity in the core is 0.01 and SNR is 2, noise would increase the AOD column density by 15.1% at some pixels and decrease it by 8.8% at others. The net effect is an increase of about 6.3% in intergrated AOD column density. Therefore, the differences between FIT and AOD column densities for Ca II may be more like the

difference seen in K I.

4. SUMMARY

Interstellar absorption was observed along 29 lines of sight in three star-forming regions, ρ Oph, Cep OB2, and Cep OB3. In this first paper, we presented high-resolution CN, CH, CH^+ , Ca I, K I, and Ca II spectra, describing the observations and data reduction. Total equivalent widths were compared with previous measurements; good agreement among determinations is the rule. The differences found for HD206165 may be the result of small-scale variation in the ISM. Our high-resolution spectra reveal complex component structure and closely blended components in most lines of sight. Reliable velocity component structure for all species was obtained by analyzing the spectra of each species for a given line of sight together. The column densities, b -values, and velocities of each component, determined by detailed profile fitting, are tabulated. Comparison of total column densities along lines of sight from the sums of component values from profile fitting and the apparent optical depth method (Savage & Sembach 1991) highlighted the robustness of the fitting results. A more detailed analysis of these results and their implications will be presented in a companion paper (Pan et al. 2003).

It is our pleasure to thank the support staff of McDonald Observatory and KPNO, especially David Doss at McDonald Observatory and Daryl Willmarth at KPNO. This research made use of the Simbad database operated at CDS Strasbourg, France. K. P. acknowledges KPNO for providing board and lodging in Tucson during observing runs. We thank the anonymous referee for suggestions that have improved the paper. The work at the University of Toledo was supported by NASA grants NAG5-4957, NAG5-8961, and NAG5-10305 and grant GO-08693.03-A from the Space Telescope Science

Institute. D.E.W. acknowledges support from NASA Long-Term Space Astrophysics grant NAG5-3228 to the University of Chicago. V.V.S. was funded through NASA Long Term Space Astrophysics grant NAG5-9213 to the University of Texas at El Paso.

A. Equivalent Width Measurements from Sandiford Data

In Table 7, we list W_λ results from the Sandiford data set for those lines of sight that were not studied at the high spectral resolution here.

REFERENCES

Allen, C. W. 1973, *Astrophysical Quantites*, London, Athlone

Allen, M. M. 1994, ApJ, 424, 754

Blaauw, A., Hiltner, W. A., & Johnson, H. L. 1959, ApJ, 130, 69

Black, J. H., & Dalgarno, A. 1977, ApJS, 34, 405

Burstein, P. R., Borken, R. J., Kranshaar, W. L., & Sanders, W. T. 1977, ApJ, 213, 405

Chaffee, F. H., & Dunham, T. 1979, ApJ, 233, 568

Chaffee, F. H., & White R. E. 1982, ApJS, 50, 169

Cox, P. L., & Smith, B. W. 1974, ApJ, 189, L105

Crane, P., Lambert, D. L., & Sheffer, Y. 1995, ApJS, 99, 107

Crawford, I. A. 1989, MNRAS, 241, 575

Daflon, S., Cunha, K., & Becker, S. 1999, ApJ, 522, 950

Daflon, S., Cunha, K., Becker, S., & Smith, V. V. 2001, ApJ, 552, 309

Danks, A. C., Federman, S. R., & Lambert, D. L. 1984, A&A, 130, 62

de Zeeuw, P. T., Brown, A. G. A., de Bruijne, J. H. J., et al. 1999, AJ, 117, 354

Elmegreen, B. G., & Lada, C. J. 1977, ApJ, 214, 725

Federman, S. R. 1982, ApJ, 257, 125

Federman, S. R., Danks, A. C., & Lambert, D. L. 1984, ApJ, 287, 219

Federman, S. R. & Glassgold, A. E. 1980, A&A, 89, 113

Federman, S. R. & Glassgold, A. E., Jenkins, E. B., & Shaya, E. J. 1980, ApJ, 242, 545

Federman, S. R., Strom, C. J., Lambert, D. L., Cardelli, J. A., Smith, V. V., & Joseph, C. L. 1994, ApJ, 424, 772

Frail, D. A., Weisberg, J. M., Cordes, J. M., & Mathers, C. 1994, ApJ, 436, 144

Garrison, R. F., & Kormendy, J. 1976, PASP, 88, 865

Gredel, R., van Dishoeck, E. F., & Black, J. H. 1991, A&A, 251, 625

Hobbs, L. M. 1984, ApJS, 56, 315

Januzzi, B. T., Black, J. H., Lada, C. J., & van Dishoeck, E. F. 1988, ApJ, 332, 995

Jenkins, E. B., & Meloy, D. A. 1974, ApJ, 193, L121

Jenniskens, P., Ehrenfreund, P., & Désert, E. X. 1992, A&A, 265, L1

Knauth, D. C., Federman, S. R., Pan, K., Yan, M., & Lambert, D. L. 2001, ApJS, 135, 201

Lambert D. L., Danks, A. C. 1986, ApJ, 340, 314

Lauroesch, J. L., & Meyer, D. M. 1999, ApJ, 519, L181

Munari, V., & Zwitter, T. 1997, A&A, 318, 269

Palazzi, E., Mandolesi, N., & Crane, P. 1992, ApJ, 398, 53

Pan, K., Sheffer, Y., Federman, S. R., & Anderson, B. G. 2003, in preparation

Pan, K., Federman, S. R., & Welty, D. E. 2001, ApJ, 558, L105

Patel, N. A., Goldsmith, P. E., & Heyer, M. H. et al. 1998, ApJ, 507, 241

Patel, N. A., Goldsmith, P. E., Snell, R. L., & Xie, T. 1995, ApJ, 447, 721

Perryman, M. A. C., ed. 1997, The *Hipparcos* and Tycho Catalogues (ESA SP-1200; Noordwijk: ESA)

Simonson, S. C. 1968, ApJ, 154, 923

Snow, T. P., Joseph, C. L., & Meyer, D. M. 1986, ApJ, 303, 433

Savage, B. D. & Sembach, K. R. 1991, ApJ, 379, 245

Tull, R. G., Macqueen, P. J., Sneden, C., & Lambert, D. L. 1995, PASP, 107, 251

van Dishoeck, E. F. & Black, J. H. 1986, ApJS, 62, 109

van Dishoeck, E. F. & Black, J. H. 1989, ApJ, 340, 273

Welty, D.E., & Fitzpatrick, E.L. 2001, ApJ, 551, L75

Welty, D. E., & Hobbs, L. M. 2001, ApJS, 133, 345

Welty, D. E., Hobbs, L. M. 2003, & Morton, D. C. ApJS, 147, 61

Welty, D. E., Hobbs, L. M., & Kulikarni, V. P. 1994, ApJ, 436, 152

Welty, D. E., Hobbs, L. M., & York, D. G. 1991, ApJS, 75, 425

Table 1. Stellar Data for Program Stars

Star	Name	Sp.	<i>V</i> (mag)	<i>l</i> ($^{\circ}$)	<i>b</i> ($^{\circ}$)	<i>E(B – V)</i> (mag)	Distance (pc)	Spectra ^a
<i>ρ</i> Oph								
HD147888	ρ Oph D	B4V	6.80	353.65	+17.71	0.48	150	M01, M01, M01
HD147932	ρ Oph C	B5V	7.27	353.65	+17.71	0.47	150	M01, M01, M01
HD147933	ρ Oph A	B2V	5.02	353.69	+17.69	0.47	150	M01 & K96, M01, M01 & K96
HD147934	ρ Oph B	B1V	5.92	353.69	+17.69	0.47	150	M01, M01, M01
Cep OB2								
HD203374A		B0IVpe	6.69	100.51	+8.62	0.60	800	M00 & K99, M00 & K99, K00
HD204827		B0V	8.00	99.17	+5.55	1.10	700	M00, M00, M01
HD206165	9 Cep	B2Ib	4.79	102.27	+7.25	0.47	950	K99, K99, M95
HD206183		B9	7.41	98.89	+3.40	0.43	750	M00, M00, M01
HD206267A		O6e	5.62	99.29	+3.74	0.51	750	K95, K95, M01
HD206267C		B0V	8.40	99.29	+3.74	0.57	750	M00, M00, M01
HD206267D		B0V	8.00	99.29	+3.73	0.44	750	M00, M00, M01
HD206773		B0Vpe	6.93	99.80	+3.62	0.50	750	M00 & K99, M00 & K99, K00
HD207198		O9IIIe	5.96	103.14	+6.99	0.61	700	K95, K96, K95
HD207260	ν Cep	A2Iab	4.30	102.31	+5.93	0.46	1150	K99, K99, M95
HD207308		B0.5V	7.49	103.11	+6.82	0.50	900	M00, M00, M01
HD207538		B0V	7.30	101.60	+4.67	0.64	850	M00, M00, M01
HD208266		B1V	8.14	102.71	+4.98	0.52	1000	M00, M00, M01
HD208440		B1V	7.91	104.03	+6.44	0.35	1150	M00, M00, M01
HD208501	13 Cep	B8Ib	5.81	100.39	+1.68	0.76	700	K99, K99, K00
HD208905		B1Vp	7.00	103.53	+5.17	0.35	800	K99, K99, K00
HD209339		B0IV	6.69	104.58	+5.87	0.37	850	K99, K99, K00
HD209481	14 Cep	O9V	5.55	102.01	+2.18	0.35	650	K99, K99, K00
HD209975	19 Cep	O9Ib	5.11	104.87	+5.39	0.35	1050	K95, K96, K95
HD210839	λ Cep	O6Iab	5.09	103.83	+2.61	0.56	800	K95, M96, M95
Cep OB3								
HD216532		O8V	8.03	109.85	+2.68	0.86	1050	M00, M00, M01
HD216898		O8.5V	8.04	109.93	+2.39	0.85	1000	M00, M00, M01

Table 1—Continued

Star	Name	Sp.	<i>V</i> (mag)	<i>l</i> ($^{\circ}$)	<i>b</i> ($^{\circ}$)	<i>E(B – V)</i> (mag)	Distance (pc)	Spectra ^a
HD217035A		B0V	7.74	110.25	+2.86	0.76	750	M00, M00, M01
HD217035B		B0V	7.74	110.25	+2.86	0.76	750	M00, M00, M01
HD217312		B0IV	7.44	110.56	+2.95	0.66	1000	M01, M01, M01

^aThe first entry is for CN and Ca II, the second for CH, CH⁺, and Ca I, the third for K I. K99 = KPNO observations in 1999, M00 = McDonald spectra in 2000, and so on.

Table 2. Total Equivalent Widths (mÅ) of CN Lines

Star (HD)	Ours			Others			Ref.
	R(0)	R(1)	P(1)	R(0)	R(1)	P(1)	
147888	5.9±0.4	2.2±0.3	1.1±0.3	7.7±2.2	<6.6	<6.6	1
147932	12.7±0.4	5.1±0.4	3.3±0.4	15.9±1.9, 7.4±2.1 ^a	6.4±1.4, <6.9 ^a	9.2±2.5, ...	1, 2
147933 ^b	6.1±0.4	1.9±0.3	1.1±0.3	6.1±0.5, 5.9±0.3	2.1±0.7, 2.5±0.3	1.1±0.6, 1.2±0.7	3, 4
	7.0	2.4	2.0				
147934	5.8±0.4	1.6±0.3	0.7±0.3	6.8±0.5	2.1±0.7	1.3±0.7	3
203374A ^b	5.8±0.6	1.8±0.6	1.0±0.5	
	6.2±1.2	<2.5	< 2.5				
204827	64.4±2.2	30.7±2.0	18.2±1.8	72.7±3.6	31.1±2.8	23.0±3.3	5
206165	6.5±0.9	<2.5	<2.5	<3	6
206183	2.4±0.5	1.3±0.4	<1.5	
206267A	19.2±0.7	6.2±0.6	3.2±0.5	18.6±0.5, 22.0	6.8±0.6, 8.0	4.1±0.5, ...	5,6
206267C	20.2±1.0	6.0±0.9	3.6±0.8	
206267D	6.5±0.8	<2.5	<2.5	
206773 ^b	0.8±0.4	<1.5	<1.5	
	<2.5	<2.5	<2.5				
207198	12.1±1.0	2.8±0.6	<2.0	12.8±1.2, 11.5±0.5, 15.0	2.8±0.8, 4.5±0.9, 4.0	2.1±1.3, ..., ...	5,5,6
207260	1.0±0.4	<1.5	<1.5	
207308	24.0±1.0	9.0±1.0	4.5±1.0	
207538	13.3±1.0	4.9±0.9	2.0±0.8	
208266	14.7±1.0	4.1±0.9	2.5±0.9	
208440	<2.0	<2.0	<2.0	
208501	29.5±1.0	12.2±1.0	5.5±1.0	
208905	<2.0	<2.0	<2.0	
209339	<2.0	<2.0	<2.0	
209481	1.0±0.4	<2.0	<2.0	
209975	<2.0	<2.0	<2.0	
210839	9.1±0.6	3.4±0.6	<2.0	8.9±0.5, 7.0	3.8±0.5, 3.0	1.9±0.6, ...	5,6
216532	7.7±1.2	3.1±1.0	< 2.0	
216898	2.3±0.8	<2.0	<2.0	
217035A	<2.0	<2.0	<2.0	
217035B	<2.0	<2.0	<2.0	

Table 2—Continued

Star (HD)	Ours			Others			Ref.
	R(0)	R(1)	P(1)	R(0)	R(1)	P(1)	
217312	2.8±0.7	<2.0	<2.0	

References. — 1) Federman unpublished; 2) Federman et al. 1994; 3) Palazzi et al. 1992; 4) Federman et al. 1984; 5) Welty unpublished; 6) Chaffee & Dunham 1979.

^a ρ Oph D instead of ρ Oph C might have been observed.

^bThe first row are measurements from McDonald observations; the second row are results from KPNO spectra.

Table 3. Total Equivalent Widths (mÅ) of CH and CH⁺ Lines

Star (HD)	CH			CH ⁺		
	Ours	Others	Ref.	Ours	Others	Ref.
147888	15.5±0.5	18.0±0.9,17.6±3.1	1,2	6.2±0.5	5.9±0.9	1
		14.0±0.6,16.3±0.5	3,3		7.2±0.8, 5.2±0.4	3,3
147932	14.3±0.3	14.1±2.8,14.8±0.9	1,2	6.0±0.6	8.7±1.6	2
147933 ^a	16.9±0.4	16.9, 16.7±0.5	4,5	12.8±0.4	12.8±0.6, 15.8,11.1±0.7,	3,4,6
				12.6		
147934	16.2±0.5	...		11.5±0.6	...	
203374A ^a	17.3±1.0	16.5±0.5	7	5.5±0.8	5.6±1.2	7
	14.8±1.7			4.3±1.5		
204827	58.9±1.5	62.2±1.3,55.4±1.5	3,7	30.3±1.8	30.0±1.1,30.0±3.0	3,7
206165	16.6±1.2	19.7±0.8,18,17.7	3,8,9	13.3±1.0	14.3±0.5,14,12.4	3,8,9
206183	14.7±1.0	14.6±1.1	7	13.3±1.0	16.0±0.7	7
206267A	23.6±0.7	22.0±0.7,17.0	7,8		12.2±0.5,13.0	7,8
206267C	21.3±1.2	21.2±0.7	7	12.1±1.2	11.4±0.8	7
206267D	20.8±1.2	20.4±0.8	7	9.4±0.9	11.8±0.6	7
206773 ^a	8.5±0.6	10.0±0.5	7	12.0±0.9	11.9±0.4	7
	7.5±1.3			12.5±1.5		
207198	27.4±1.0	27.6±0.8,29.9±0.8	3,3	18.2±1.5	17.1±0.7, 15.5±0.8	3,3
		26.0, 28.7±1.2	8,9		15.6±1.2	9
207260	13.7±1.0	16.9±0.8	3	15.6±1.5	16.0±0.6	3
207308	23.7±1.0	22.1±0.5	7	14.0±1.3	15.1±0.5	7
207538	28.0±1.2	30.8±0.7,27.1±0.5	3,7	7.0±0.9	7.8±0.7,6.6±0.7	3,7
208266	25.5±1.2	23.6±0.9	7	4.5±0.6	4.2±0.5	7
208440	9.7±1.0	11.5±2.0	7	7.4±0.8	6.6±1.8	7
208501	34.3±1.6	...		3.0±1.1	...	
208905	7.4±1.2	10.6±1.2	7	4.4±1.2	7.6±0.5	7
209339	6.2±1.2	9.3±0.6,5.0±0.7	7,9	6.2±1.5	10.6±0.8,8.8±0.7	7,9
209481	5.9±1.0	9.2±0.4	7	4.0±0.8	3.8±0.4	7
209975	6.6±1.3	8.3±1.2	10	19.0±1.3	22.1,20.1±1.0	3,10
210839	...	16.5	4	...	12.1	4
216532	15.9±1.3	...		35.1±1.7	...	
216898	22.3±1.5	...		22.6±1.7	...	

Table 3—Continued

Star (HD)	CH			CH ⁺		
	Ours	Others	Ref.	Ours	Others	Ref.
217035A	11.2±1.2	...		18.0±1.4	...	
217035B	8.6±1.2	...		30.5±1.7	...	
217312	19.1±1.0	...		39.1±1.7	...	

References. — 1) Federman et al. 1994; 2) Federman unpublished; 3) Welty unpublished; 4) Crane et al. 1995; 5) Danks et al. 1984; 6) Lambert & Danks 1986; 7) Sandiford data; 8) Chaffee & Dunham 1979; 9) Jenniskens et al. 1992; 10) Allen 1994.

^aThe first row are measurements from McDonald observations; the second row are results from KPNO spectra.

Table 4. Total Equivalent Widths (mÅ) of Ca I, Ca II, and K I lines

Star (HD)	Ca I			Ca II			K I		
	Ours	Others	Ref.	Ours	Others	Ref.	Ours	Others	Ref.
147888	5.5±0.5	6.4±0.9, 5.8±0.4	1,2	63.6±3.0	60.7±2.4	1	87.9±3.0	92.0±2.0, 87.3±0.6	1,2
	...				54.8±1.6, 54.7±2.9	2,2		85.6±1.2	2
147932	4.7±0.5	3.1±0.7	1	61.1±2.0	59.7±3.6	1	77.8±3.0	...	
147933 ^a	4.7±0.3	5.0±2.0, 4.5±0.6	3,4	62.4±2.0	...		85.7±2.0	87.91±4	5,6
	5.7±0.6	4.8±0.4	8	57.9±1.1	...		87.3±1.2	86.0±1.6, 85.4±0.8	2,10
147934	4.5±0.4	...		63.7±2.5	...		85.7±3.0	85.0	5
203374A ^a	8.1±1.0	10.0±1.5	7	266.9±4.0	
	7.9±1.8	...		266.5±7.0	...		148.9±4.0	...	
204827	6.5±1.0	10.7±3.1	7	263.8±6.0	243±7	2	304.8±4.0	309.3±3.1	2
206165	7.8±1.2	7.5±1.0, 12.1±1.0	8,8	248.1±6.0	240.7±2.0, 237.1±1.7	2,2	191.1±3.0	189.7±3.0, 192.4±1.6	2,10
	...	12	9	...	321	9	
206183	7.5±1.0	9.6±1.5	7	229.2±5.0	...		172.8±3.0	...	
206267A	...	9.3±0.5, <3	7,9	248.5±4.0	248.9±1.5, 236	2,9	199.7±3.0	204.8±2.3, 198.1±1.3	2,10
206267C	8.4±1.0	10.6±1.0	7	252.9±6.0	...		202.9±3.0	...	
206267D	7.9±1.0	9.5±0.5	7	253.6±6.0	...		192.7±3.0	...	
206773 ^a	4.9±0.8	5.5±0.5	7	202.1±4.0	
	5.0±1.5	...		199.7±7.0	...		98.5±4.0	...	
207198	12.4±1.3	12.7±1.7, 15.3±0.7	8,8	313.8±8.0	314.5±4.4, 311.1±3.9	2,2	238.9±4.0	240.1±1.2, 236.7±1.7	2,10
	...	15.0	9	...	277 ^b	9	
207260	17.6±1.3	14.0±1.3, 16.2±0.7	8,8	186.7±8.0	215.0±3.8	2	203.6±3.0	221±13, 206.6±1.0	6,10
207308	4.2±0.6	4.6±0.5	7	251.5±5.0	...		136.7±3.0	...	
207538	9.9±1.0	12.2±1.3, 11.8±1.0	2,7	227.9±5.0	...		211.1±3.0	...	
208266	7.3±1.0	6.7±0.8	7	182.4±6.0	...		175.4±5.0	...	
208440	5.7±1.0	...		272.9±5.0	...		142.2±3.0	...	
208501	2.8±0.7	...		218.8±8.0	241.1±5.2	2	163.3±3.0	166.2±2.6	2
208905	<3.0	4.5±0.9	7	218.5±8.0	...		84.5±3.0	...	
209339	2.0±0.7	6.4±0.5	7	187.1±8.0	...		115.5±4.0	...	
209481	<3.0	4.7±0.5	7	254.5±8.0	262.7±3.4	2	81.9±3.0	79.0±3.1	2
209975	7.1±1.0	7.0±1.6, 7.2±1.0	8,12	240.9±6.0	243.6±2.4, 260	2,12	92.9±3.0	102.4±2.7, 95.1±2.5	2,10
210839	10.4±0.9	10.4±0.9, 9.0	8,9	238.8±4.0	240.0±1.8, 218	2,9	157.0±2.5	165.9±3.1, 174.2±4.3	2,2
	...	9.2	12	...	250	12	...	157.0±2.0, 161.6	10,10

Table 4—Continued

Star (HD)	Ca I			Ca II			K I		
	Ours	Others	Ref.	Ours	Others	Ref.	Ours	Others	Ref.
216532	5.5±1.0	...		290.4±6.0	...		234.9±4.0	...	
216898	9.5±1.2	...		282.9±6.0	...		228.1±4.0	...	
217035A	1.2±0.5	...		271.2±8.0	...		191.6±3.0	...	
217035B	2.0±0.6	...		280.8±8.0	...		159.4±3.0	160	13
217312	7.3±1.0	...		276.9±5.0	...		183.0±3.0	...	

References. — 1) Federman unpublished; 2) Welty unpublished; 3) Snow et al. 1986; 4) Lambert & Danks 1986; 5) Lauroesch & Meyer 1999; 6) Chaffee & White 1982; 7) Sandiford data; 8) Welty et al. 2003; 9) Chaffee & Dunham 1979; 10) Welty & Hobbs 2001; 11) Allen 1994; 12) Hobbs 1984; 13) Munari & Zwitter 1997.

^aThe first row are measurements from McDonald observations; the second row are results from KPNO spectra.

^bComponents at $V_{LSR} = -35$ to -70 km s $^{-1}$ might not be included in the measurement.

Table 5. Component Measurements of Interstellar Lines

Table 5—Continued

Table 5—Continued

V_{LSR}^a	CN		CH		CH ⁺		Ca I		K I		Ca II	
	N^b	b^a	N^b	b^a	N^b	b^a	N^b	b^a	N^b	b^a	N^b	b^a
	(10 ¹²)		(10 ¹²)		(10 ¹²)		(10 ⁹)		(10 ¹¹)		(10 ¹¹)	
-21.6		1.1	1.5
-18.4		1.5	2.0
-15.2		1.3	1.7
-13.2		1.4	1.5
-11.2		0.2	0.8	2.0	1.5
-9.9	...		3.6	0.9		3.0	0.7	2.7	1.5
-8.6		0.1	0.8	2.9	1.4
-6.2		3.3	1.6	...		0.7	1.0	6.2	1.5
-4.3		4.5	0.8	0.8	0.7	7.5	1.5
-2.9	...		2.0	0.8	2.2	1.9	5.0	0.8	1.0	0.7	3.3	1.5
-1.3	0.7	0.9	5.0	0.9	2.9	1.9	7.3	0.6	3.1	0.6	11.2	1.6
0.3	1.2	0.7	5.7	1.1	...		3.0	1.1	2.5	0.7	3.2	1.3
2.0		5.2	1.7	3.3	1.1	1.1	0.6	11.2	1.4
3.7	0.5	0.9	4.1	1.1	...		6.4	1.0	3.9	1.0	2.4	1.3
5.1		2.3	1.7	...		0.1	1.0	2.5	1.4
6.4		1.5	1.0
HD206183												
-24.0		0.4	2.0
-18.8		1.4	2.2
-14.6		1.8	2.1
-10.6		1.8	2.5
-6.3		2.3	0.8	0.5	0.9	3.8	2.0
-4.6	...		1.5	1.2	1.4	1.9	2.1	0.8	0.4	0.6	2.0	2.1
-1.6	1.0	0.9	7.8	1.2	10.5	2.1	4.6	0.9	6.4	1.1	11.2	2.3
-0.1	...		1.3	1.2	2.0	2.0	3.3	0.9	0.9	1.0	0.4	2.0
1.3	...		2.6	1.2	...		3.3	1.0	2.6	1.1	11.4	1.9
3.2	...		1.4	1.1	1.2	2.0	5.7	1.1	2.5	1.1	9.9	1.9
4.5	...		1.5	1.1	...		5.2	1.1	0.9	1.1	2.9	1.9
6.9		0.1	0.7	1.2	1.8

Table 5—Continued

V_{LSR}^a	CN		CH		CH ⁺		Ca I		K I		Ca II	
	N^b	b^a	N^b	b^a	N^b	b^a	N^b	b^a	N^b	b^a	N^b	b^a
	(10^{12})		(10^{12})		(10^{12})		(10^9)		(10^{11})		(10^{11})	
9.9	...		2.0	1.2	...		3.5	1.1	0.8	1.2	3.7	1.4
13.5		0.4	1.6
16.1		0.3	0.9
HD206267A ^c												
-23.3		1.2	1.8
-20.6		1.4	1.5
-17.8		2.2	1.5
-14.9		1.7	1.8
-12.3		1.5	1.8
-8.8	0.1	0.9	2.3	1.5
-6.3		4.8	1.5
-4.7	0.3	0.7	4.1	1.1	3.8	1.0	3.8	1.6
-2.7	7.0	0.7	8.8	1.2	6.0	1.1	4.4	1.5
-0.9	0.9	0.7	2.1	1.2	1.4	1.0	7.8	1.5
0.9	0.5	0.8	9.0	1.0	3.7	1.2	11.6	1.5
2.4	...		2.0	1.2	1.2	1.0	7.1	1.6
4.2	...		4.3	1.1	3.2	1.0	4.8	1.5
7.0	0.1	0.6	2.3	1.6
10.8		1.2	2.0
HD206267C												
-25.0		0.3	1.7
-23.1		0.4	2.0
-21.1		2.0	2.3
-17.5		2.4	2.3
-15.0		2.0	2.4
-12.2		1.0	2.0
-8.8	0.1	0.7	3.3	2.2
-6.1		3.8	2.0

Table 5—Continued

Table 5—Continued

V_{LSR}^a	CN		CH		CH ⁺		Ca I		K I		Ca II	
	N^b	b^a	N^b	b^a	N^b	b^a	N^b	b^a	N^b	b^a	N^b	b^a
	(10^{12})		(10^{12})		(10^{12})		(10^9)		(10^{11})		(10^{11})	
-19.5		0.4	1.6
-17.3		0.5	1.5
-13.5		0.6	1.4
-11.1		0.4	1.5
-9.1		1.6	1.4
-6.4		1.5	1.1	3.2	1.5
-5.2	...		1.6	1.1	1.2	2.1	5.0	1.2	0.8	0.9	4.7	1.5
-3.0		2.5	2.4	1.2	1.1	0.6	0.7	3.1	1.4
-0.9	0.45	0.8	4.5	0.9	...		3.4	0.9	3.0	0.7	8.5	1.5
0.8		0.5	1.5
2.3	...		5.1	1.2	9.2	2.2	5.3	1.1	1.4	0.7	15.6	1.4
5.0		1.9	2.4	1.1	0.7	0.5	0.6	5.2	1.3
7.4		2.5	1.6
13.1		0.4	1.9
HD207198 ^d												
-28.3		0.3	1.5
-23.5		0.4	1.3
-19.7		0.4	1.7
-18.1		0.8	1.7
-15.8		1.6	1.0
-14.2		1.5	1.5
-11.8		2.1	1.5
-9.9		4.0	1.8
-8.1		0.7	1.1	3.7	1.5
-6.2	1.3	0.7	5.3	1.2	3.1	2.0	...		3.1	0.8	8.8	1.5
-4.1	...		2.9	0.9	3.9	2.0	4.4	1.0	1.3	0.6	8.5	1.4
-2.1	2.4	0.9	10.1	1.1	2.0	1.9	5.4	0.9	7.0	1.3	10.2	1.5
-0.2	0.9	1.0	9.8	1.1	7.9	2.1	6.7	0.9	5.8	1.0	13.7	1.5
3.1	...		3.0	0.9	2.5	2.1	10.9	0.7	2.8	0.7	15.9	2.6

Table 5—Continued

Table 5—Continued

V_{LSR}^a	CN		CH		CH ⁺		Ca I		K I		Ca II	
	N^b	b^a	N^b	b^a	N^b	b^a	N^b	b^a	N^b	b^a	N^b	b^a
	(10 ¹²)		(10 ¹²)		(10 ¹²)		(10 ⁹)		(10 ¹¹)		(10 ¹¹)	
-12.4		1.6	1.6
-9.1		0.1	0.6	4.3	1.6
-6.4	...		2.2	1.2	4.1	2.2	2.5	1.0	0.6	0.9	10.2	1.7
-4.3	...		2.9	1.2	5.0	2.3	3.4	1.1	2.7	0.9	6.2	1.4
-2.4	9.0	1.0	18.4	1.0	2.0	2.0	4.4	1.0	8.2	1.1	6.8	1.5
-0.5	2.0	0.9	8.6	1.1	5.4	2.2	2.7	1.0	3.2	0.9	7.0	1.4
2.1		0.2	0.7	6.5	2.1
4.3		0.2	0.6	2.8	1.3
7.3		0.3	1.6
HD207538												
-20.3		0.3	1.7
-17.5		0.5	1.5
-15.3		0.3	1.5
-13.8		0.5	1.6
-12.4		0.7	1.8
-9.0		3.0	2.0
-6.5	...		2.1	1.1	1.9	1.9	3.5	1.0	1.1	1.0	3.5	1.5
-4.4	0.6	0.8	7.0	1.0	1.3	1.9	9.0	1.1	8.3	1.3	19.5	1.5
-2.5	1.5	0.9	11.7	0.9	1.5	1.9	8.4	1.1	6.4	0.7	8.2	1.4
-0.5	1.8	0.9	11.8	1.1	1.2	2.1	6.2	1.2	7.4	1.3	10.0	1.6
1.9	0.9	0.8	4.4	0.8	2.0	2.1	5.6	1.2	1.3	0.8	15.8	1.6
4.4	...		1.1	0.9	1.0	1.9	5.7	1.2	0.6	0.7	7.7	1.3
6.6		2.0	1.0	0.2	0.9	3.3	1.4
8.7		0.9	0.9	0.1	0.8	1.1	1.6
HD208266												
-11.0		0.8	1.8
-9.0		0.2	0.6	0.1	1.5
-7.2	...		0.4	1.0		0.1	0.9	1.6	1.5

Table 5—Continued

Table 5—Continued

Table 5—Continued

Table 5—Continued

Table 5—Continued

V_{LSR}^a	CN		CH		CH ⁺		Ca I		K I		Ca II	
	N^b	b^a	N^b	b^a	N^b	b^a	N^b	b^a	N^b	b^a	N^b	b^a
	(10^{12})		(10^{12})		(10^{12})		(10^9)		(10^{11})		(10^{11})	
-5.0		1.1	0.7	0.4	0.9	4.6	1.4
-2.3	2.6	0.8		3.1	1.2	4.0	0.6	6.0	1.4
-0.4	0.9	0.8		7.7	0.9	4.4	0.6	11.5	1.4
1.7		4.1	1.0	0.9	0.8	8.8	1.7
3.3		6.8	1.0	0.7	1.0	14.1	1.7
5.7		3.3	1.5
7.5		2.8	1.1	0.8	0.6	3.3	1.4
10.4		7.4	0.6	1.0	0.6	3.3	1.2
14.4		0.2	1.9
HD216532												
-17.7		7.5	1.4	...		1.9	0.7	1.7	1.7
-15.3		0.6	2.0
-13.8		6.3	1.6	...		0.5	1.5	3.0	2.0
-10.5	...		1.9	0.9	9.6	2.0	...		1.0	1.1	5.3	1.9
-8.0		6.5	1.9	...		0.4	0.9	4.2	1.8
-6.5		4.2	2.1	...		0.3	1.1	6.1	1.7
-4.3		5.2	1.2	3.2	1.5	10.0	1.9
-2.5		3.5	1.8
-0.8	...		3.0	1.1	5.2	2.0	2.7	1.1	1.2	1.1	5.3	1.8
0.8		2.8	0.6	6.5	1.8
3.4	3.1	0.7	11.2	1.0	3.0	2.0	...		3.1	1.0	4.9	1.8
5.1	...		1.8	1.1	2.7	2.0	3.6	0.9	1.1	1.1	8.2	1.8
8.6	...		2.3	0.8	...		4.5	1.0	2.7	1.2	8.6	1.5
11.6		0.3	1.4
14.4		1.2	2.1
HD216898												
-24.6		0.9	1.5
-20.1		0.2	0.9	0.7	1.8

Table 5—Continued

Table 5—Continued

V_{LSR}^a	CN		CH		CH ⁺		Ca I		K I		Ca II	
	N^b	b^a	N^b	b^a	N^b	b^a	N^b	b^a	N^b	b^a	N^b	b^a
	(10 ¹²)		(10 ¹²)		(10 ¹²)		(10 ⁹)		(10 ¹¹)		(10 ¹¹)	
-25.0		0.9	1.8
-18.1		0.6	1.8
-14.3	...		7.5	0.9	12.0	2.2	...		4.2	1.5	4.7	1.7
-11.1	...		3.6	1.1	8.8	2.1	...		1.3	1.3	5.8	1.4
-6.9		7.1	2.2	...		2.2	1.0	12.3	1.5
-3.4		0.9	0.8	4.9	1.6
-1.3		6.3	1.0	1.3	1.3	12.1	1.7
1.0		2.5	1.9
2.8		0.7	1.0	8.2	1.9
5.7		5.6	2.3	...		0.2	1.0	4.5	1.5
8.6		0.3	0.7	6.1	1.6
HD217312												
-25.1		0.7	2.0
-20.6		0.9	1.9
-15.1	...		2.1	1.2	5.1	2.1	1.6	1.1	0.9	1.0	1.0	1.4
-12.0	...		1.1	1.1	2.4	2.1	1.7	1.1	0.5	0.8	2.8	1.4
-9.0	...		3.2	1.2	8.6	2.2	2.5	1.2	1.0	1.0	4.9	1.5
-7.1		4.0	2.0	2.6	1.0	0.5	1.0	5.0	1.5
-5.0	...		3.0	1.1	5.6	2.2	2.9	1.1	1.5	1.2	8.7	1.6
-2.1	...		1.7	0.9	4.5	2.2	2.9	1.0	1.7	1.3	7.4	1.7
0.0	0.4	0.9	1.6	1.5	2.5	1.8	2.6	1.0	0.7	1.1	8.2	1.9
2.2		2.4	2.2		2.2	1.5
5.2	0.5	1.0	4.2	1.5	2.8	2.2	4.0	1.0	2.5	0.8	9.8	2.1
7.2	0.6	0.8	8.1	1.3	8.3	2.2	5.0	1.3	5.0	1.1	9.6	2.1
10.4	...		0.6	1.1	0.8	1.9	1.3	0.7	...		2.2	1.6
13.4		0.4	2.0

^ain the unit of km s⁻¹.^bin the unit of cm⁻².^cNo available CH⁺ and Ca I data for this line of sight.^dCa II components at $V_{LSR} < 40$ km s⁻¹ are not included.^eNo available CH and CH⁺ data for this line of sight.

Table 6. Total Column Densities

Star	CN		CH		CH ⁺		Ca I		Ca II		K I	
	(×10 ¹² cm ⁻²)		(×10 ¹² cm ⁻²)		(×10 ¹² cm ⁻²)		(×10 ⁹ cm ⁻²)		(×10 ¹¹ cm ⁻²)		(×10 ¹¹ cm ⁻²)	
	FIT	AOD	FIT	AOD	FIT	AOD	FIT	AOD	FIT	AOD	FIT	AOD
HD147888	2.1	2.1	21.8	21.2	7.5	7.2	20.2	19.8	19.4	14.9	11.0	8.7
HD147932	6.0	5.9	19.2	19.2	7.0	6.7	16.2	16.5	19.2	15.5	8.0	6.7
HD147933	2.1	2.1	23.7	23.6	15.9	15.7	17.4	17.6	17.5	14.1	10.3	8.4
HD147934	2.0	1.9	23.3	23.2	14.3	14.1	16.9	17.0	19.6	13.9	10.9	8.6
HD203374A	2.2	2.1	22.2	22.0	7.1	7.0	30.4	29.8	66.7	64.5	13.9	11.8
HD204827	37.4	37.2	87.9	86.4	36.9	37.3	25.0	23.8	61.9	60.8	42.0	36.4
HD206165	2.4	2.4	20.5	20.7	15.9	15.5	29.5	28.9	62.0	58.8	16.5	14.3
HD206183	1.0	1.0	18.2	18.1	15.1	14.8	30.1	29.0	52.8	51.0	15.2	14.1
HD206267A	8.7	8.5	30.2	29.7	58.2	56.5	19.8	18.5
HD206267C	7.9	7.8	28.2	27.8	15.1	14.7	30.4	30.2	61.9	59.8	21.8	19.2
HD206267D	2.5	2.4	27.3	28.0	11.8	11.7	28.7	27.7	58.7	57.5	19.3	16.7
HD206773	0.45	0.4	11.2	11.3	14.7	14.6	16.0	16.1	47.7	45.6	7.8	7.0
HD207198	4.6	4.5	35.4	34.9	22.1	21.9	44.7	43.4	83.5	80.7	25.2	22.7
HD207260	0.45	0.46	15.2	15.0	19.1	18.8	68.7	68.2	41.6	39.7	19.5	16.8
HD207308	11.0	10.9	32.2	32.0	16.5	16.1	15.1	13.6	54.5	52.8	15.2	13.4
HD207538	4.9	4.9	38.1	37.8	8.8	8.5	41.3	40.7	74.4	64.1	25.4	21.2
HD208266	5.7	5.7	33.6	33.3	5.1	5.1	25.8	26.0	42.1	40.6	21.9	18.4
HD208440	<0.9	...	11.7	11.7	8.7	8.6	20.2	19.5	57.8	56.6	10.0	9.6
HD208501	13.7	13.5	49.9	49.7	3.6	3.4	9.6	9.5	60.2	59.6	22.6	17.7
HD208905	<0.9	...	5.4	5.8	6.0	5.9	<4.0	...	45.8	44.9	6.2	5.8
HD209339	<0.9	...	7.9	8.1	6.6	6.6	6.7	6.6	43.4	42.4	8.4	8.0
HD209481	0.45	0.4	6.7	6.6	5.3	5.2	<4.0	...	63.4	60.2	5.8	5.6
HD209975	<0.9	...	8.5	8.4	24.2	24.0	23.2	23.5	59.3	58.4	6.2	6.1
HD210839	3.5	3.4	37.3	37.0	62.3	60.1	13.8	13.0
HD216532	3.1	3.2	20.2	19.1	45.0	44.3	16.0	16.0	69.4	68.3	18.2	16.9
HD216898	0.8	0.8	28.1	27.9	26.5	26.2	31.1	31.2	72.7	69.6	17.8	16.9
HD217035A	<0.9	...	16.8	16.3	20.9	20.4	4.1	4.1	60.2	58.1	14.6	13.6
HD217035B	<0.9	...	11.1	10.8	33.5	34.0	6.3	6.2	63.3	60.4	11.1	10.9
HD217312	1.5	1.4	25.5	25.2	47.1	46.8	27.1	27.0	63.8	62.1	14.3	13.5

Table 7. Results from Sandiford Data

Star	$W_\lambda(\text{CH})$ (mÅ)	V_{LSR} (km s ⁻¹)	$W_\lambda(\text{CH}^+)$ (mÅ)	V_{LSR} (km s ⁻¹)	$W_\lambda(\text{Ca I})$ (mÅ)	V_{LSR} (km s ⁻¹)
HD239649	10.4 ± 0.8	-9.4	5.5 ± 0.8	-9.2
	12.3 ± 1.1	-0.6	13.7 ± 0.8	+4.6	4.1 ± 0.8	+1.3
HD239676	16.5 ± 1.0	-2.8	13.0 ± 0.9	-1.5	5.1 ± 1.2	-3.7
	20.7 ± 1.0	+3.4	7.0 ± 0.9	+5.7	6.1 ± 1.2	+5.0
HD239681	14.4 ± 1.5	-0.1	22.2 ± 1.5	-3.4	4.0 ± 1.7	-0.6
HD205794	22.3 ± 0.8	-8.2	35.7 ± 1.2	-8.9	2.0 ± 0.6	-5.4
	10.7 ± 0.9	+1.3	7.5 ± 1.1	+3.0	5.5 ± 0.6	+3.0
HD239710	22.9 ± 1.1	+1.9	8.0 ± 1.1	+0.9	4.6 ± 1.4	+1.8
	2.2 ± 1.1	+12.3	8.0 ± 1.1	+8.0
HD205948	17.7 ± 0.7	-0.4	a	...	a	...
	4.0 ± 0.7	+7.2	a	...	a	...
HD239712	25.5 ± 0.6	+0.2	9.0 ± 0.7	-1.9	6.1 ± 0.7	+1.6
HD206081	3.5 ± 1.1 ^b	-5.1
	21.8 ± 0.9	+0.8	6.3 ± 0.6	+1.6	8.3 ± 1.2	+3.5
	7.0 ± 0.6 ^b	+8.7
HD239724	11.6 ± 0.8	+2.3	17.2 ± 1.0	+4.5	1.9 ± 1.1	+4.3
HD206327	10.9 ± 0.5	-2.6	10.6 ± 0.5	-1.7	9.3 ± 0.8	-1.5
HD239729	27.7 ± 0.9	+0.6	6.3 ± 0.9	+1.9	8.8 ± 0.7	+2.8
HD239738	28.4 ± 1.0	+1.7	18.4 ± 1.3	+1.1	5.2 ± 1.3	+4.9

Table 7—Continued

Star	$W_{\lambda}(\text{CH})$ (mÅ)	V_{LSR} (km s ⁻¹)	$W_{\lambda}(\text{CH}^+)$ (mÅ)	V_{LSR} (km s ⁻¹)	$W_{\lambda}(\text{Ca I})$ (mÅ)	V_{LSR} (km s ⁻¹)
HD239742	16.4 ± 0.6	+4.3	5.1 ± 0.7	+3.1	3.6 ± 1.1	+6.9
	4.3 ± 0.8 ^b	+10.7
HD239743	46.1 ± 1.6	+0.0	8.2 ± 1.5	-2.1	7.2 ± 1.2	+2.2
HD239745	18.7 ± 1.0	+1.8	13.6 ± 1.5	+2.5	7.3 ± 3.2	+5.6
	5.1 ± 1.0	+8.1
HD239748	18.1 ± 0.6	+2.2	17.1 ± 0.7	+4.3	4.4 ± 0.6	+5.5
HD239767	6.9 ± 0.9	-7.6	7.9 ± 1.4	-7.8
	24.6 ± 1.1	+0.1	12.7 ± 1.5	-0.2	14.8 ± 1.2	-2.4
	4.4 ± 1.3 ^b	+7.8
HD235618	15.4 ± 0.9	-6.2	13.7 ± 1.3	-4.9	10.9 ± 1.7	-2.3
	20.3 ± 0.8	+2.3	7.2 ± 1.0	+4.7
HD207951	9.3 ± 0.5	-5.5	7.0 ± 0.6	-3.8	4.9 ± 0.4	-2.2
	2.5 ± 0.5	+3.5	3.2 ± 0.7	+3.3	1.2 ± 0.4	+8.9
HD209454	8.3 ± 0.5	-0.9	1.9 ± 0.7	-4.6	9.0 ± 0.7	-1.4
	7.4 ± 0.5	+5.4	4.4 ± 0.7	+2.5	4.5 ± 0.9	+6.7
HD213023	28.8 ± 1.1	-6.4	37.3 ± 1.2	-3.8	11.7 ± 1.5	-5.2
	12.5 ± 1.1	+3.6	4.2 ± 1.5	+5.7
HD213757	5.5 ± 0.7	-12.8	3.8 ± 0.5	-12.0
	7.2 ± 0.5	+1.2	13.5 ± 0.5	+2.4	4.8 ± 1.1	+2.1

^aLine contaminated by cosmic ray hit.^bPossibly a stellar feature.

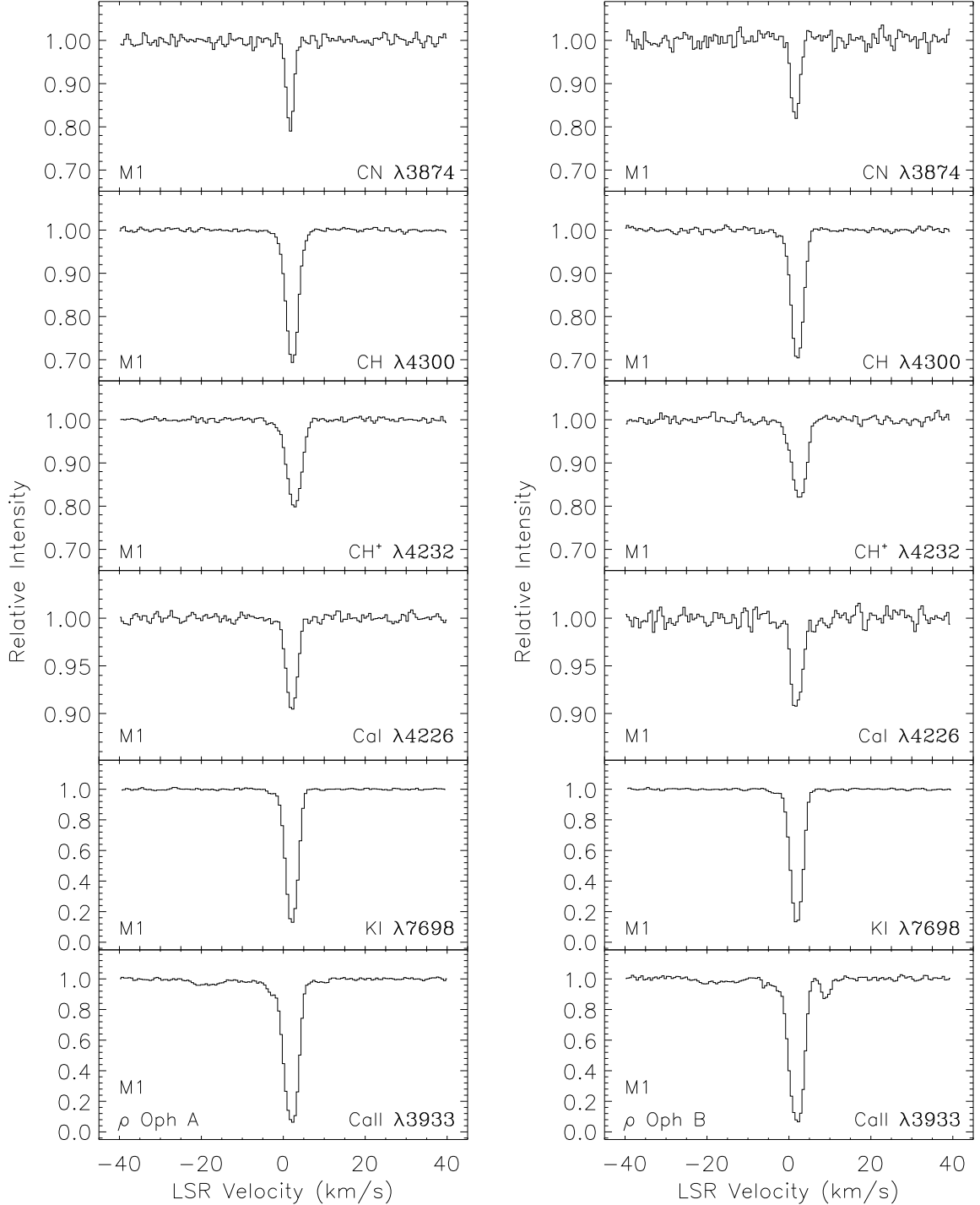


Fig. 1.— Interstellar CN, CH, CH⁺, Ca I, K I, and Ca II absorption profiles toward ρ Oph A and ρ Oph B. The transition is given in the lower-right corner of each panel. The source of the spectra is denoted M1, M2, and K. M1 represents observations from McDonald Observatory during 2000 and 2001, whereas M2 denotes observations in 1995 and 1996 from McDonald Observatory with a higher resolution. All KPNO spectra are denoted K. Note that the vertical scales differ from panel to panel.

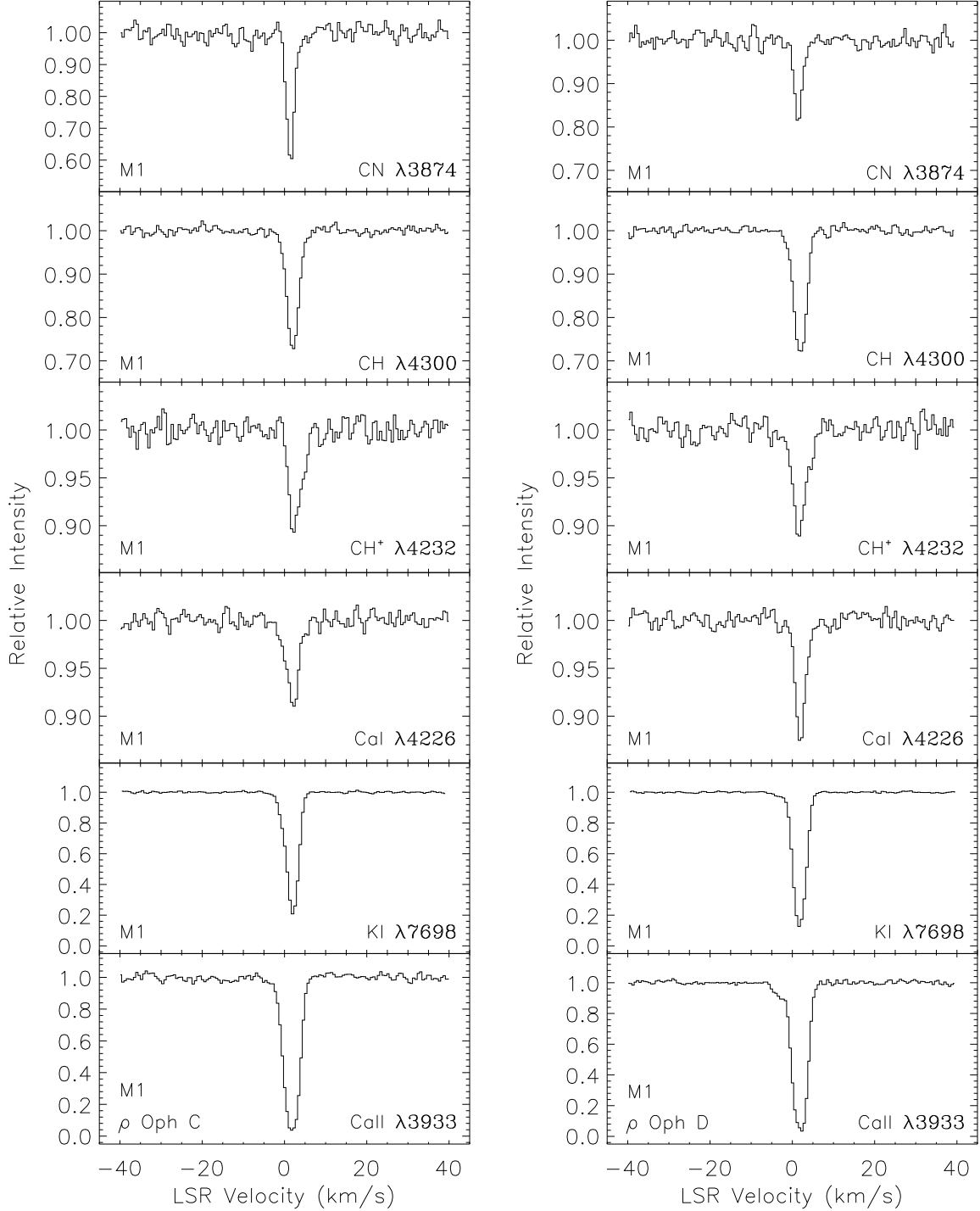


Fig. 2.— Interstellar CN, CH, CH⁺, Ca I, K I, and Ca II absorption profiles toward ρ Oph C and ρ Oph D (as for Figure 1).

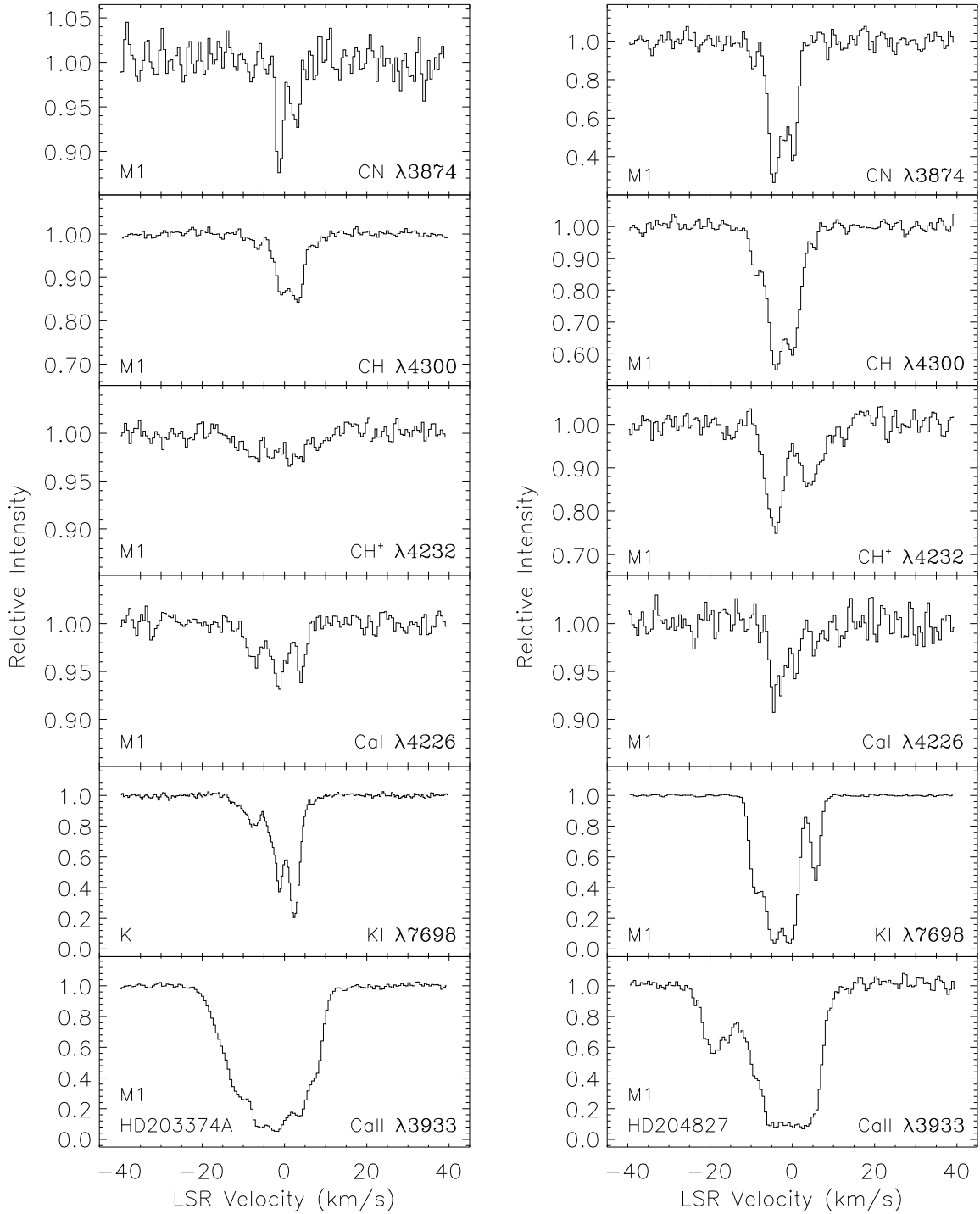


Fig. 3.— Interstellar CN, CH, CH^+ , Ca I, K I, and Ca II absorption profiles toward HD203374A and HD204827 (as for Figure 1).

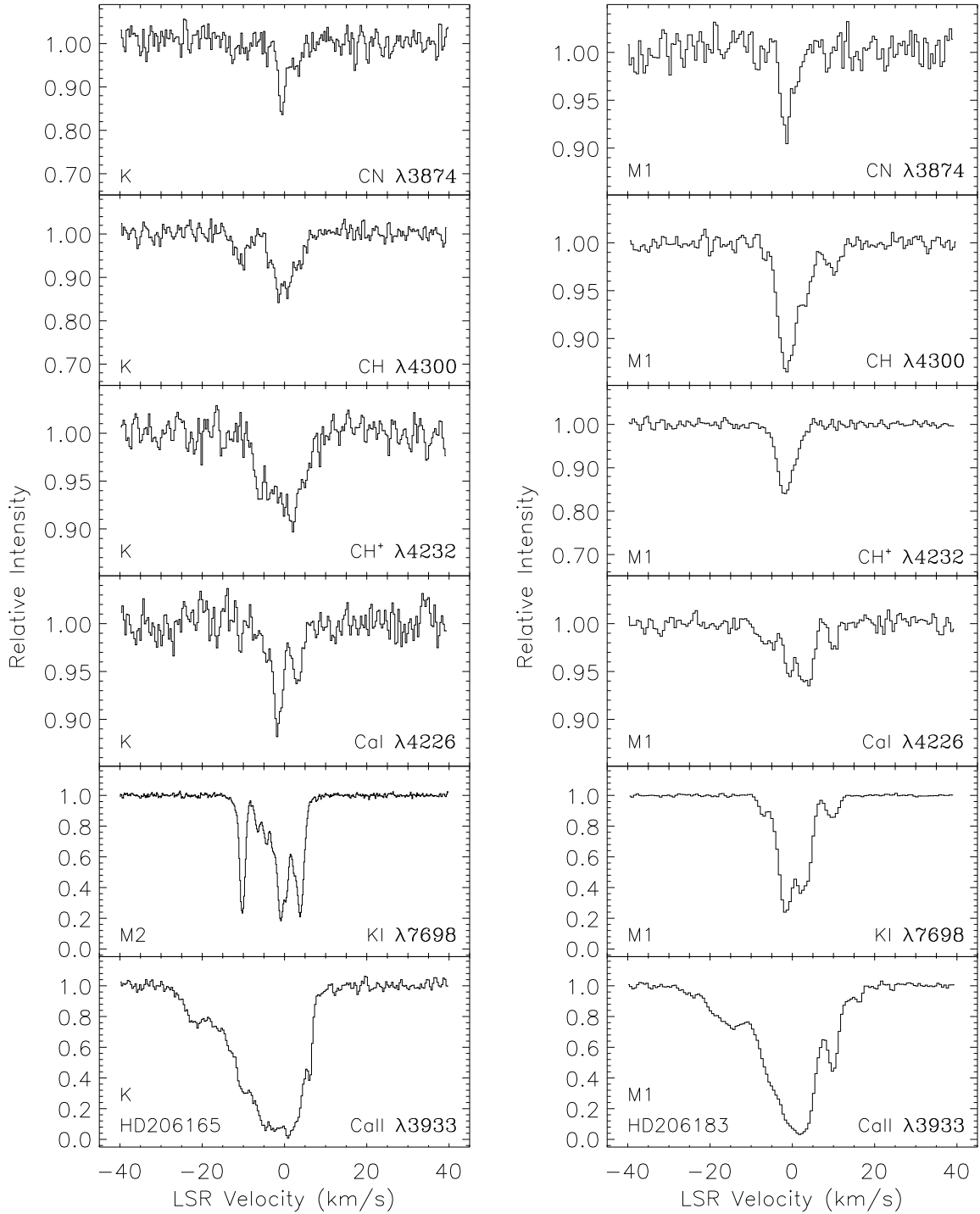


Fig. 4.— Interstellar CN, CH, CH⁺, Ca I, K I, and Ca II absorption profiles toward HD206165 and HD206183 (as for Figure 1).

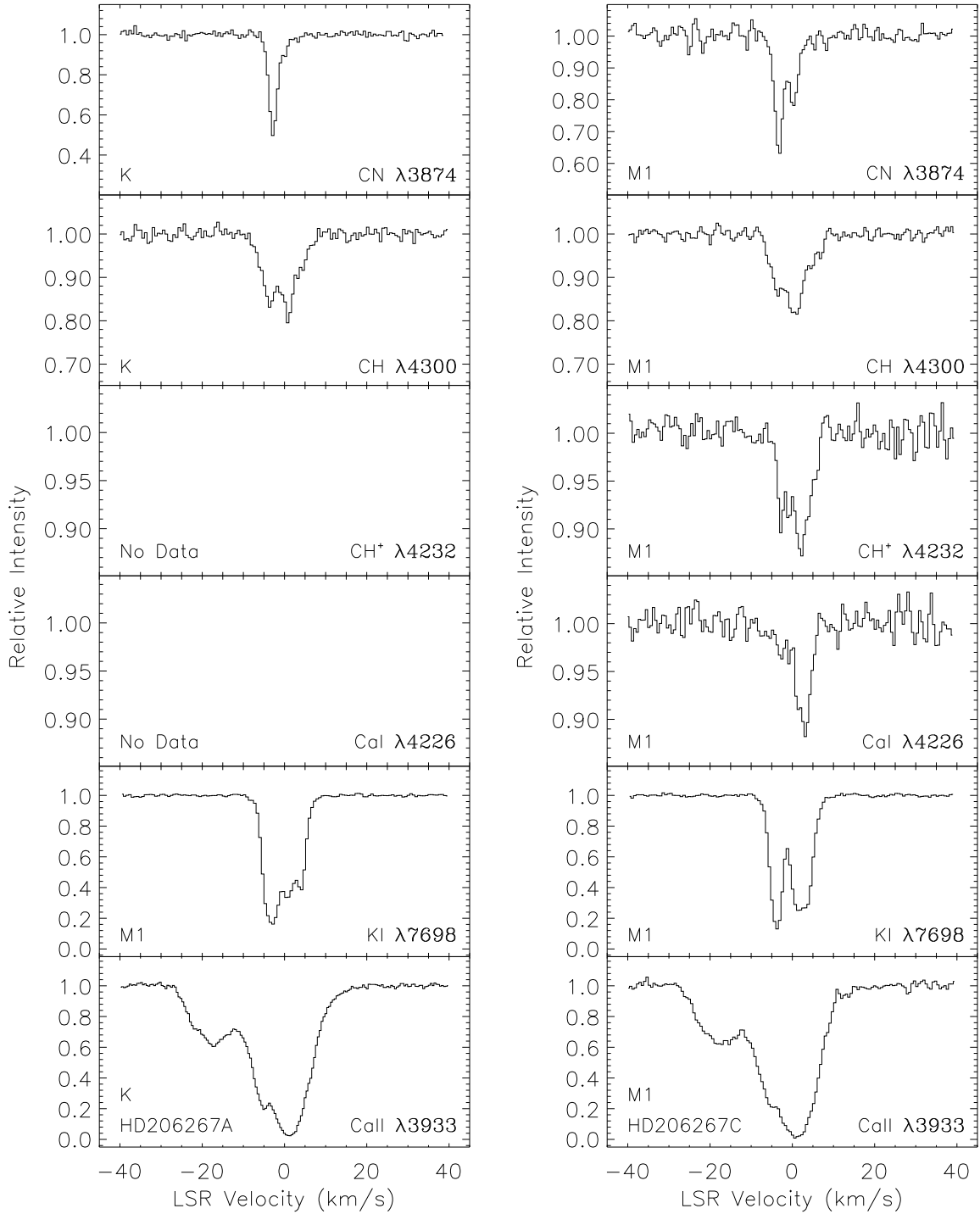


Fig. 5.— Interstellar CN, CH, CH^+ , Ca I, K I, and Ca II absorption profiles toward HD206267A and HD206267C (as for Figure 1).

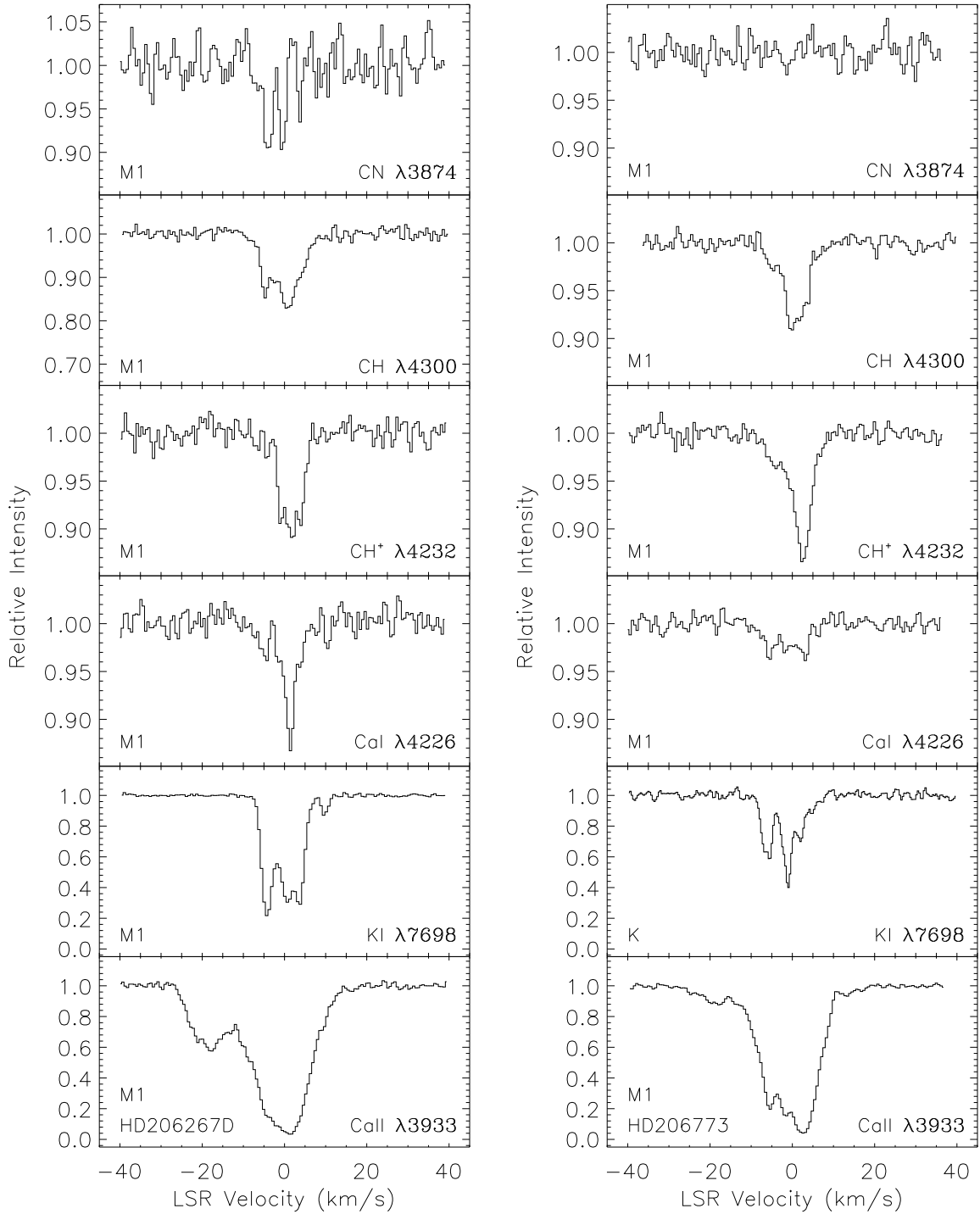


Fig. 6.— Interstellar CN, CH, CH^+ , Ca I, K I, and Ca II absorption profiles toward HD206267D and HD206773 (as for Figure 1).

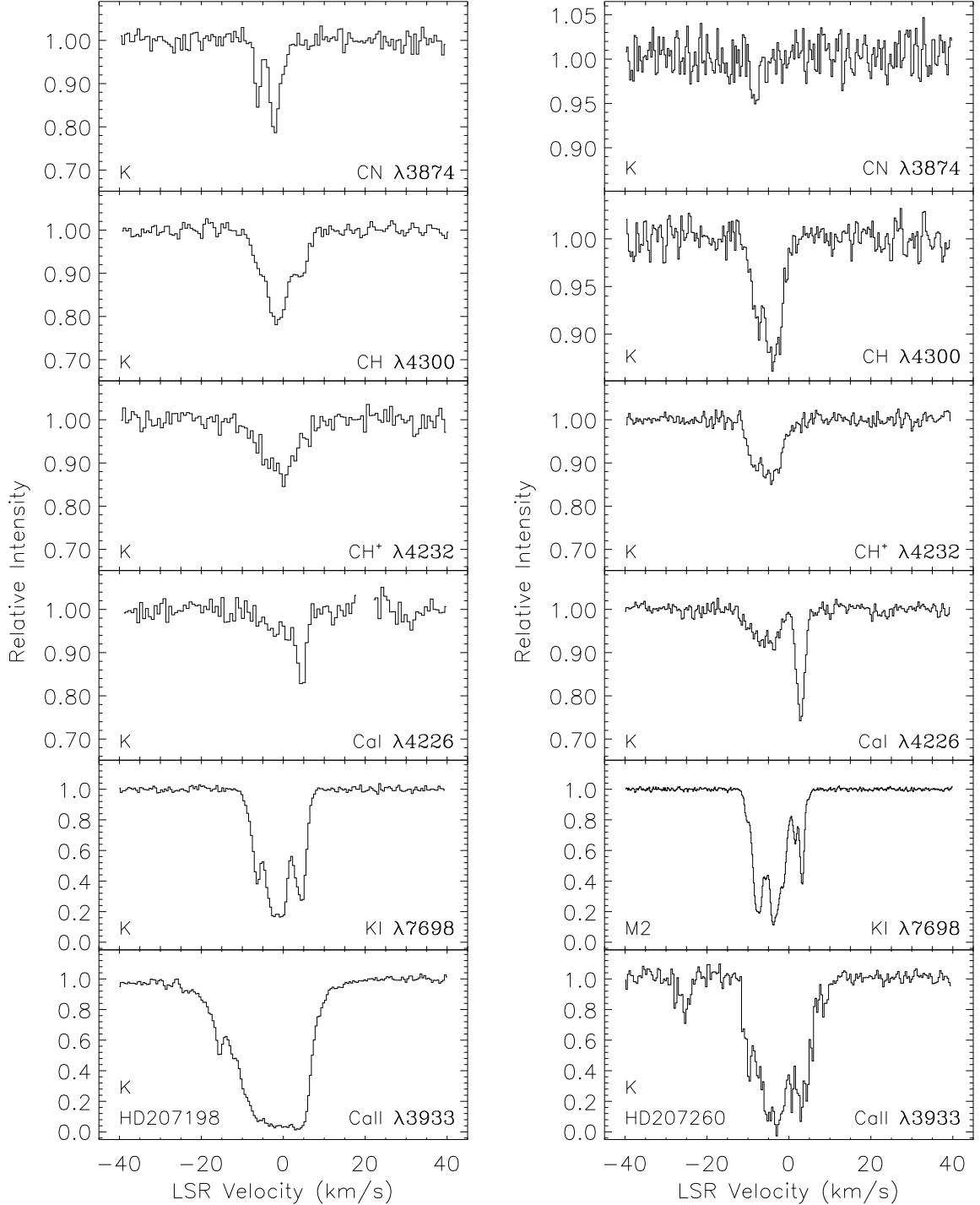


Fig. 7.— Interstellar CN, CH, CH^+ , Ca I, K I, and Ca II absorption profiles toward HD207198 and HD207260 (as for Figure 1). Blank region for Ca I toward HD207198 contains bad pixels.

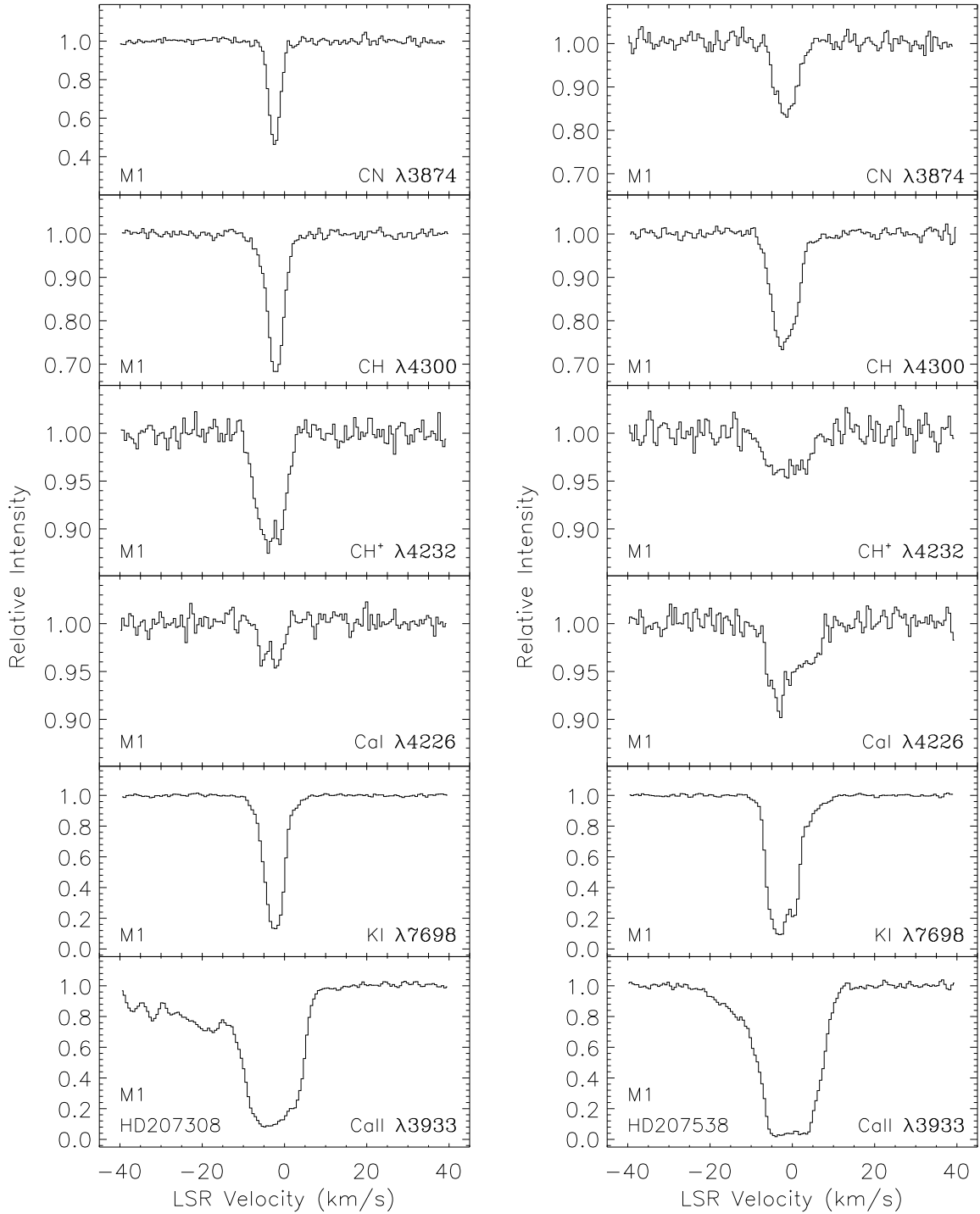


Fig. 8.— Interstellar CN, CH, CH^+ , Ca I, K I, and Ca II absorption profiles toward HD207308 and HD207538 (as for Figure 1).

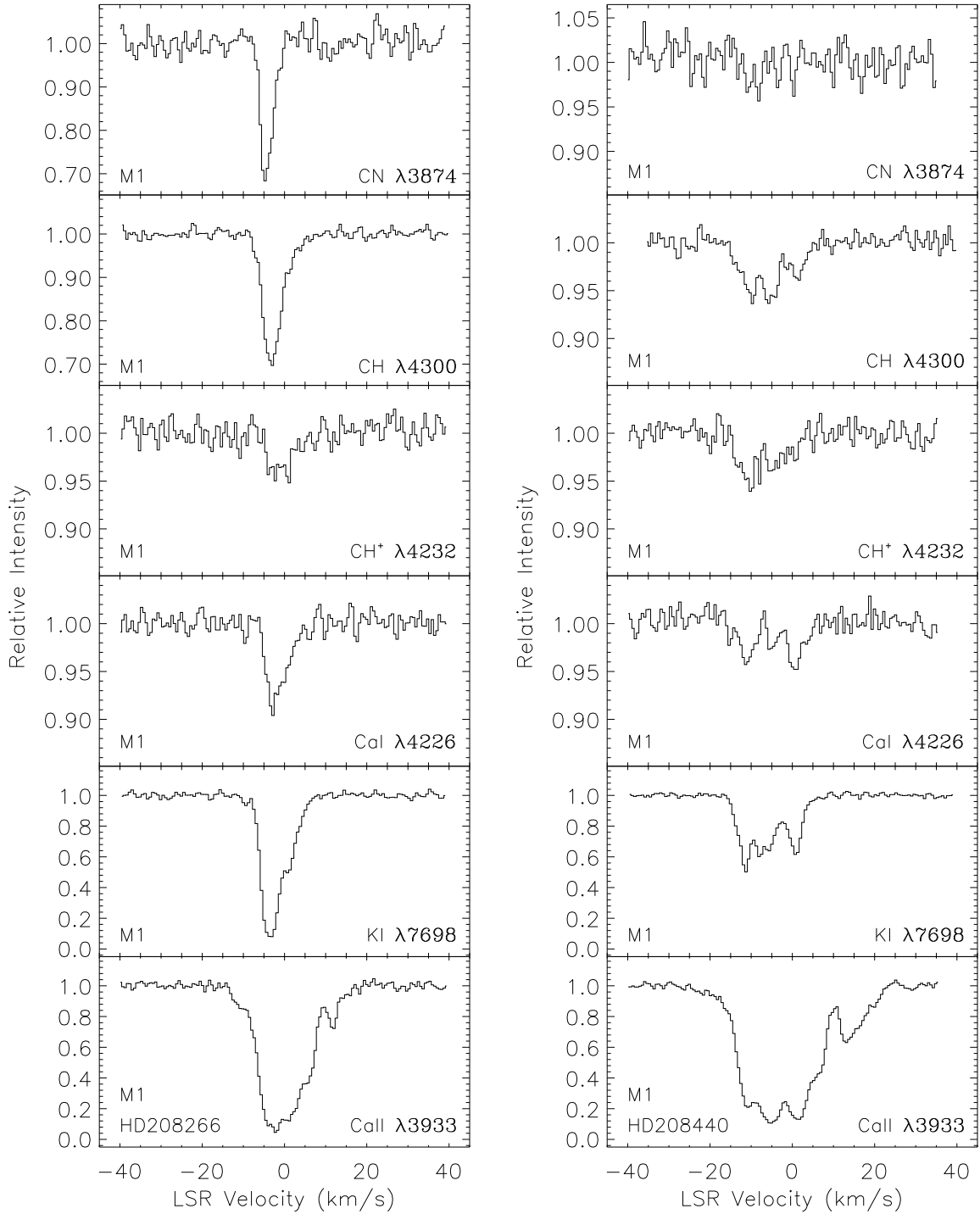


Fig. 9.— Interstellar CN, CH, CH^+ , Ca I, K I, and Ca II absorption profiles toward HD208266 and HD208440 (as for Figure 1).

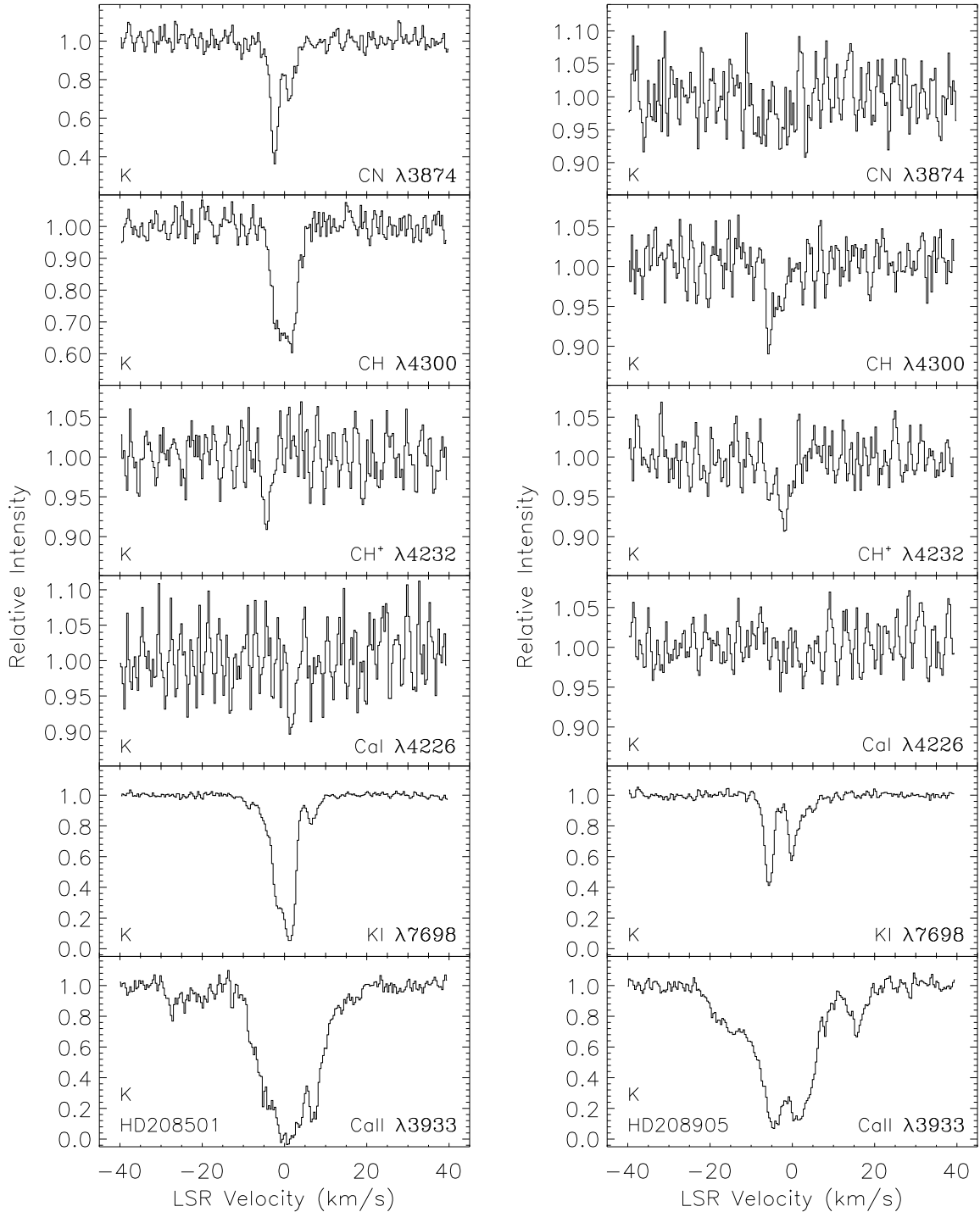


Fig. 10.— Interstellar CN, CH, CH⁺, Ca I, K I, and Ca II absorption profiles toward HD208501 and HD208905 (as for Figure 1).

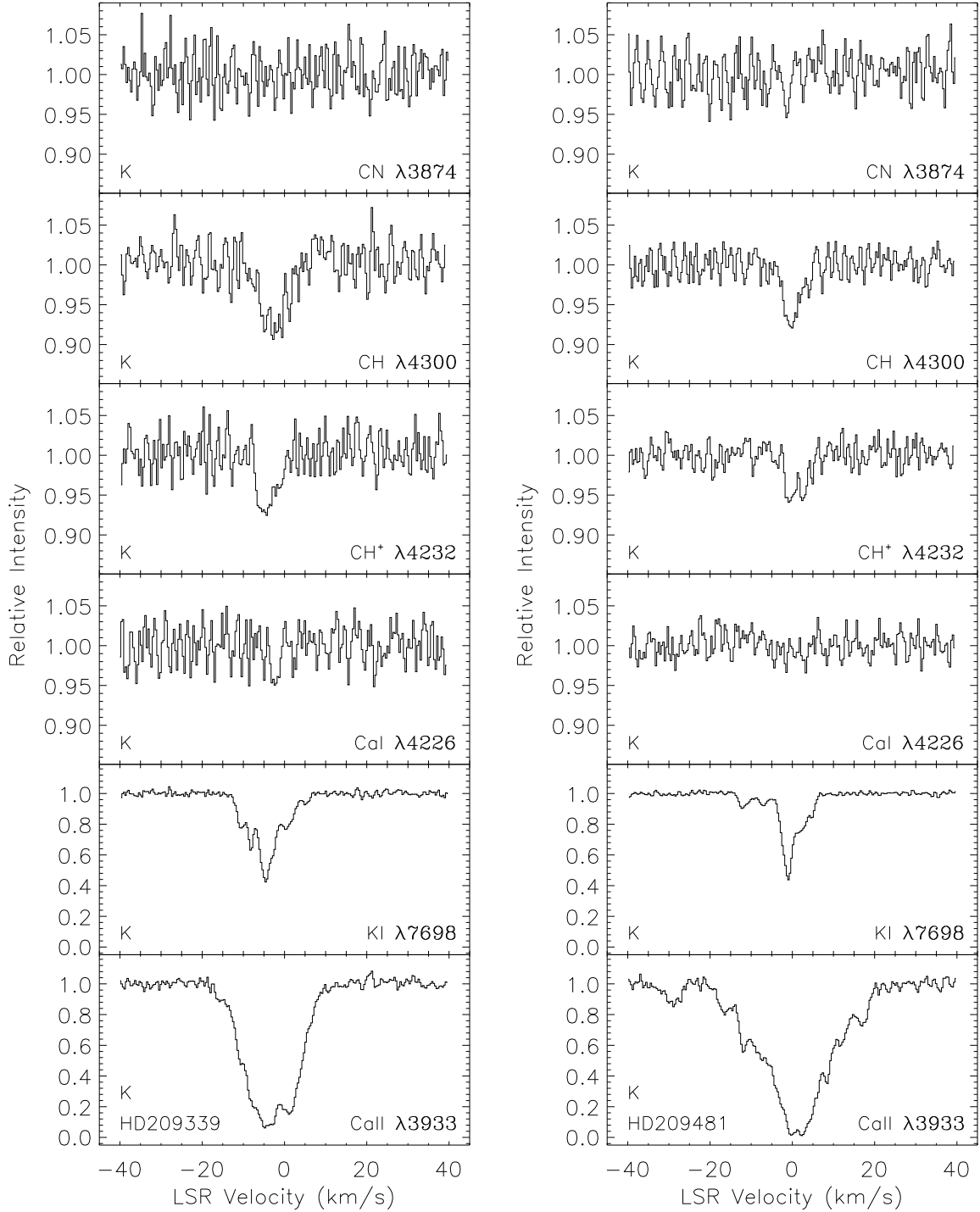


Fig. 11.— Interstellar CN, CH, CH⁺, Ca I, K I, and Ca II absorption profiles toward HD209339 and HD209481 (as for Figure 1).

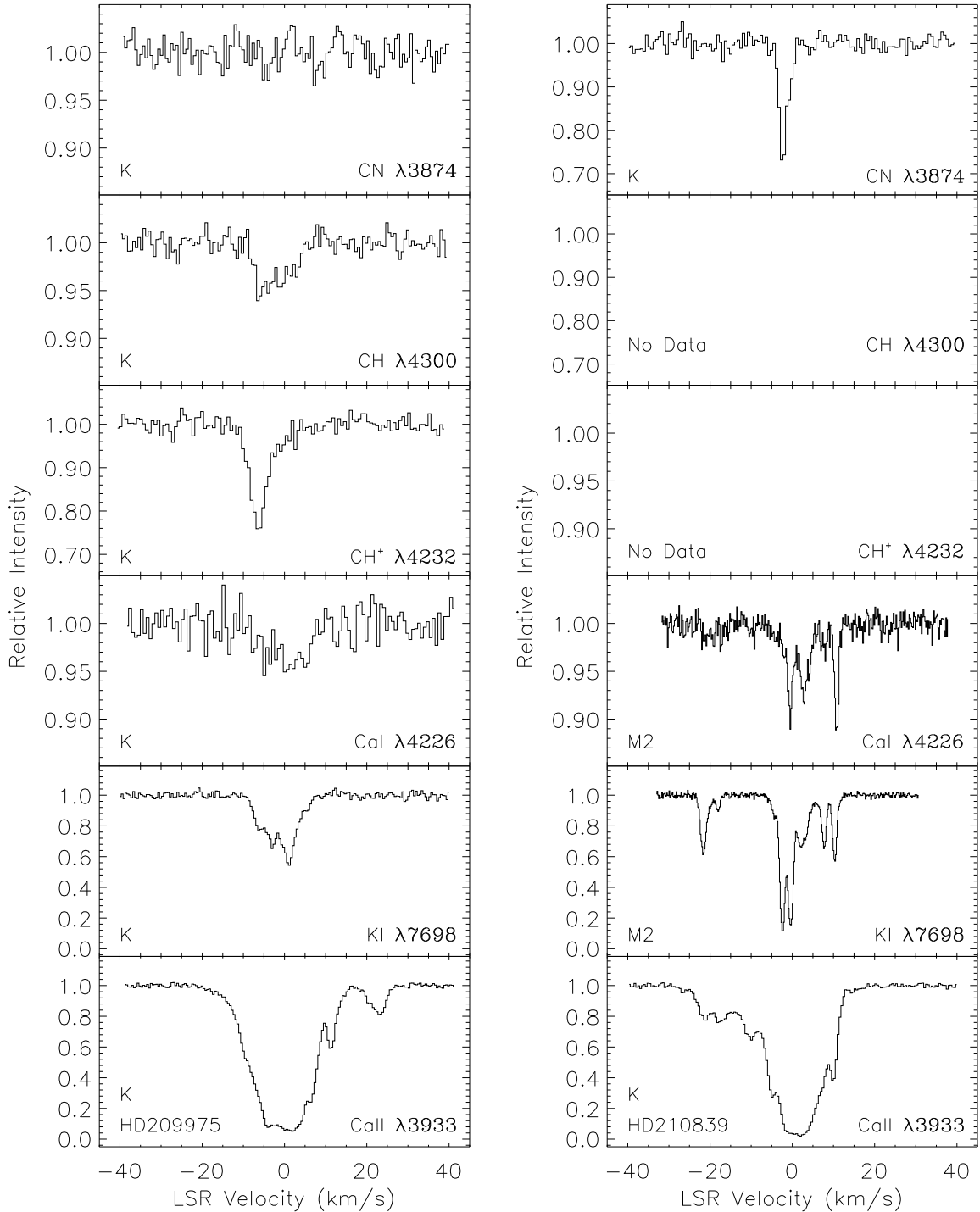


Fig. 12.— Interstellar CN, CH, CH⁺, Ca I, K I, and Ca II absorption profiles toward HD209975 and HD210839 (as for Figure 1).

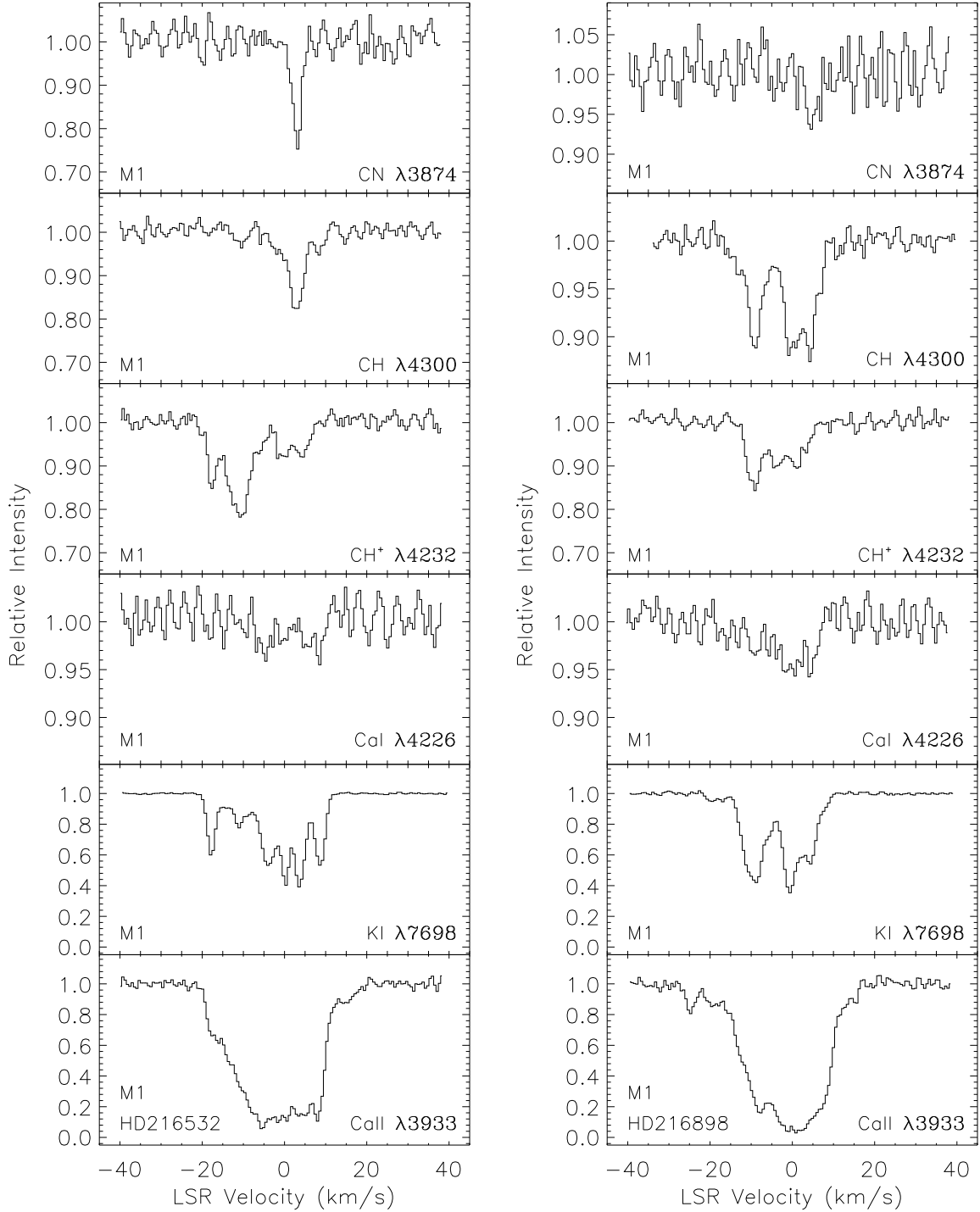


Fig. 13.— Interstellar CN, CH, CH⁺, Ca I, K I, and Ca II absorption profiles toward HD216532 and HD216898 (as for Figure 1).

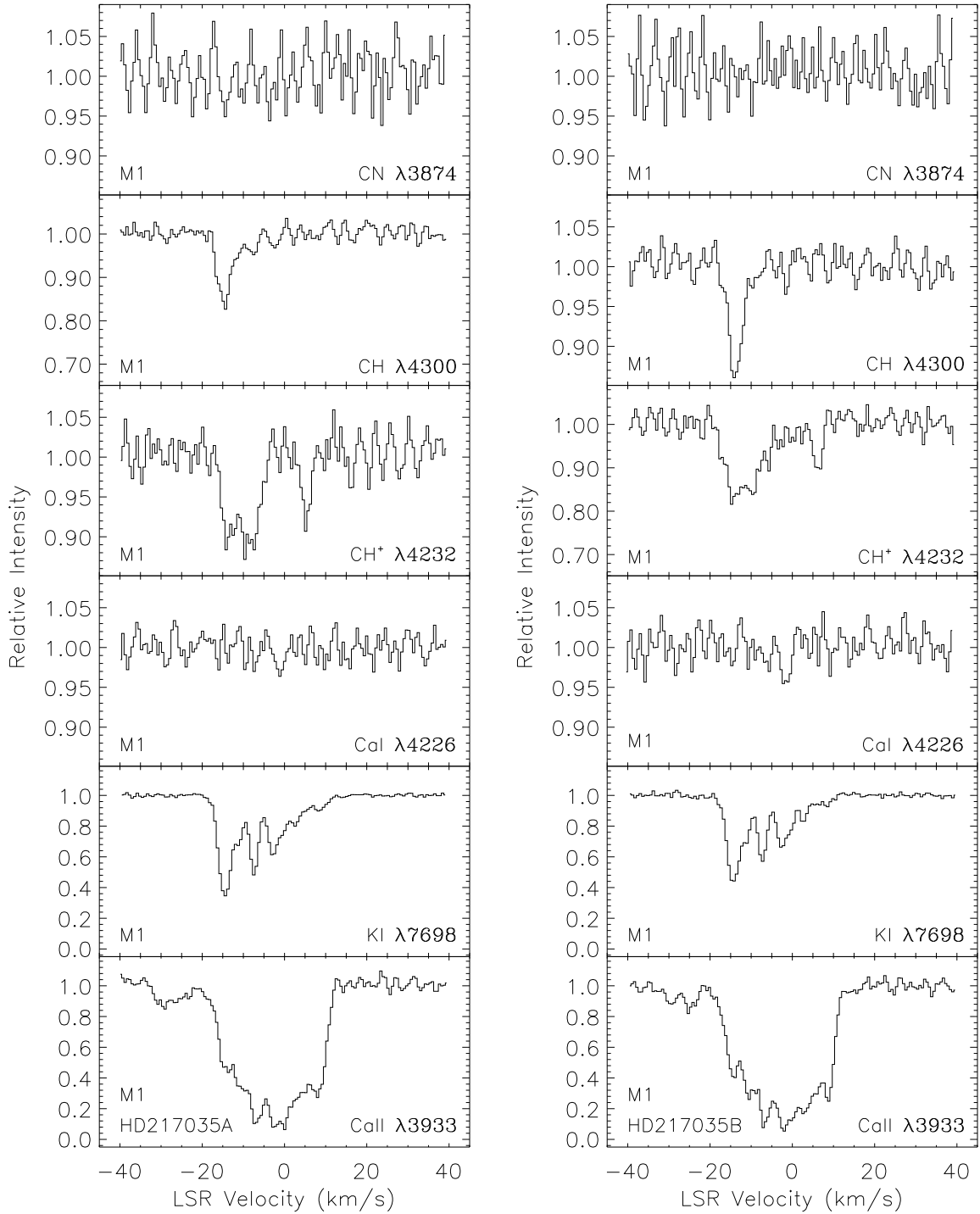


Fig. 14.— Interstellar CN, CH, CH⁺, Ca I, K I, and Ca II absorption profiles toward HD217035A and HD217035B (as for Figure 1).

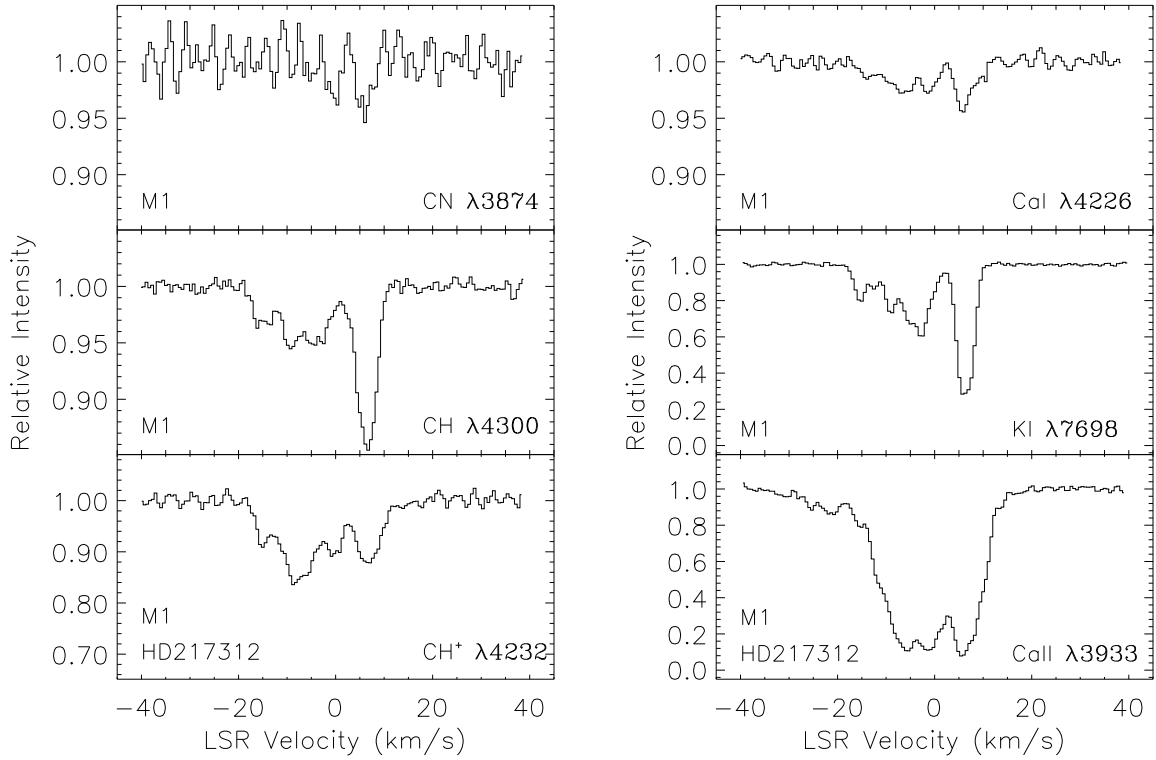


Fig. 15.— Interstellar CN, CH, CH⁺, Ca I, K I, and Ca II absorption profiles toward HD217312 (as for Figure 1).